



Chinese Pharmaceutical Association  
Institute of Materia Medica, Chinese Academy of Medical Sciences

Acta Pharmaceutica Sinica B

[www.elsevier.com/locate/apsb](http://www.elsevier.com/locate/apsb)  
[www.sciencedirect.com](http://www.sciencedirect.com)



ORIGINAL ARTICLE

# ASF1A-dependent P300-mediated histone H3 lysine 18 lactylation promotes atherosclerosis by regulating EndMT



Mengdie Dong<sup>a,†</sup>, Yunjia Zhang<sup>b,†</sup>, Minghong Chen<sup>b,†</sup>, Yongkang Tan<sup>b</sup>,  
Jiao Min<sup>b</sup>, Xian He<sup>b</sup>, Fuhao Liu<sup>c</sup>, Jiaming Gu<sup>b</sup>, Hong Jiang<sup>b</sup>,  
Longbin Zheng<sup>b,d</sup>, Jiajing Chen<sup>b</sup>, Quanwen Yin<sup>b</sup>, Xuesong Li<sup>b</sup>,  
Xiang Chen<sup>b</sup>, Yongfeng Shao<sup>e,\*</sup>, Yong Ji<sup>f,g,\*</sup>, Hongshan Chen<sup>a,h,i,\*</sup>

<sup>a</sup>Department of Cardiovascular Surgery, the First Affiliated Hospital of Nanjing Medical University, and Key Laboratory of Cardiovascular and Cerebrovascular Medicine, School of Pharmacy, National Vaccine Innovation Platform, Nanjing Medical University, Nanjing 211166, China

<sup>b</sup>Key Laboratory of Cardiovascular and Cerebrovascular Medicine, School of Pharmacy, Nanjing Medical University, Nanjing 211166, China

<sup>c</sup>Department of Clinical Medicine, Nanjing Medical University TIANYUAN Honors School, Nanjing Medical University, Nanjing 211166, China

<sup>d</sup>Department of Anesthesiology, Sir Run Run Hospital, Nanjing Medical University, Nanjing 211166, China

<sup>e</sup>Department of Cardiovascular Surgery, the First Affiliated Hospital of Nanjing Medical University, Nanjing 211166, China

<sup>f</sup>Key Laboratory of Cardiovascular and Cerebrovascular Medicine, Key Laboratory of Targeted Intervention of Cardiovascular Disease, Collaborative Innovation Center for Cardiovascular Disease Translational Medicine, State Key Laboratory of Reproductive Medicine, School of Pharmacy, the Affiliated Suzhou Hospital of Nanjing Medical University, Gusu School, Nanjing Medical University, Nanjing 211166, China

<sup>g</sup>National Key Laboratory of Frigid Zone Cardiovascular Diseases (NKLFZCD), Department of Pharmacology (State-Province Key Laboratories of Biomedicine-Pharmaceutics of China), College of Pharmacy, Key Laboratory of Cardiovascular Medicine Research and Key Laboratory of Myocardial Ischemia, Chinese Ministry of Education, NHC Key Laboratory of Cell Transplantation, the Central Laboratory of the First Affiliated Hospital, Harbin Medical University, Harbin 150081, China

<sup>h</sup>Key Laboratory of Targeted Intervention of Cardiovascular Disease, Collaborative Innovation Center for Cardiovascular Disease Translational Medicine, Nanjing Medical University, Nanjing 211166, China

<sup>i</sup>Department of Cardiology, Huai'an First People's Hospital Affiliated with Nanjing Medical University, Huai'an 223399, China

Received 18 October 2023; received in revised form 11 January 2024; accepted 28 February 2024

\*Corresponding authors.

E-mail addresses: [hongshanchen@njmu.edu.cn](mailto:hongshanchen@njmu.edu.cn) (Hongshan Chen), [yongji@hrbmu.edu.cn](mailto:yongji@hrbmu.edu.cn) (Yong Ji), [shaoyongfeng@njmu.edu.cn](mailto:shaoyongfeng@njmu.edu.cn) (Yongfeng Shao),

<sup>†</sup>These authors made equal contributions to this work.

Peer review under the responsibility of Chinese Pharmaceutical Association and Institute of Materia Medica, Chinese Academy of Medical Sciences.

<https://doi.org/10.1016/j.apsb.2024.03.008>

2211-3835 © 2024 The Authors. Published by Elsevier B.V. on behalf of Chinese Pharmaceutical Association and Institute of Materia Medica, Chinese Academy of Medical Sciences. This is an open access article under the CC BY-NC-ND license (<http://creativecommons.org/licenses/by-nc-nd/4.0/>).

## KEY WORDS

Histone lactylation;  
Atherosclerosis;  
Endothelial-to-mesenchymal transition;  
ASF1A;  
SNAIL1;  
Endothelial dysfunction;  
Lactate;  
Epigenetic

**Abstract** Endothelial-to-mesenchymal transition (EndMT) is a key driver of atherosclerosis. Aerobic glycolysis is increased in the endothelium of atheroprone areas, accompanied by elevated lactate levels. Histone lactylation, mediated by lactate, can regulate gene expression and participate in disease regulation. However, whether histone lactylation is involved in atherosclerosis remains unknown. Here, we report that lipid peroxidation could lead to EndMT-induced atherosclerosis by increasing lactate-dependent histone H3 lysine 18 lactylation (H3K18la) *in vitro* and *in vivo*, as well as in atherosclerotic patients' arteries. Mechanistically, the histone chaperone ASF1A was first identified as a cofactor of P300, which precisely regulated the enrichment of H3K18la at the promoter of *SNAIL1*, thereby activating *SNAIL1* transcription and promoting EndMT. We found that deletion of ASF1A inhibited EndMT and improved endothelial dysfunction. Functional analysis based on *ApoE*<sup>KO</sup>*Asf1a*<sup>ECKO</sup> mice in the atherosclerosis model confirmed the involvement of H3K18la in atherosclerosis and found that endothelium-specific ASF1A deficiency inhibited EndMT and alleviated atherosclerosis development. Inhibition of glycolysis by pharmacologic inhibition and advanced PROTAC attenuated H3K18la, *SNAIL1* transcription, and EndMT-induced atherosclerosis. This study illustrates precise crosstalk between metabolism and epigenetics *via* H3K18la by the P300/ASF1A molecular complex during EndMT-induced atherogenesis, which provides emerging therapies for atherosclerosis.

© 2024 The Authors. Published by Elsevier B.V. on behalf of Chinese Pharmaceutical Association and Institute of Materia Medica, Chinese Academy of Medical Sciences. This is an open access article under the CC BY-NC-ND license (<http://creativecommons.org/licenses/by-nc-nd/4.0/>).

## 1. Introduction

As the leading cause of cardiovascular diseases (CVDs), atherosclerosis is a typical chronic inflammatory vascular disease, resulting in a high rate of morbidity and mortality worldwide<sup>1,2</sup>. Endothelial cells (ECs), which continuously line the lumen of blood vessels, play a pivotal role in maintaining the barrier function of the vasculature. Endothelial dysfunction is a well-known essential initiating event involved in atherosclerosis<sup>3,4</sup>. However, the underlying mechanism of endothelial dysfunction remains to be further verified.

Endothelial-to-mesenchymal transition (EndMT) is a cellular transition progression in which ECs are transformed into mesenchymal cells in response to multiple stimuli and gradually lose endothelial-specific markers and acquire a mesenchymal phenotype<sup>5</sup>. The process of EndMT is precisely regulated by several transcription factors, including *SNAIL1*, *SLUG*, *TWIST1*, *ZEB1*, etc., which repress endothelial marker gene expression and activate the expression of mesenchymal genes<sup>6</sup>. EndMT plays an essential role in cardiac development and maintaining valve tissue homeostasis<sup>7</sup>. Nonetheless, abnormal EndMT is involved in a variety of disease processes, including pulmonary hypertension, myocardial fibrosis, and cancer<sup>6</sup>. Recently, the abnormal occurrence of EndMT, which often occurs in atherosclerosis-prone regions of arteries, has been identified as a key driver of endothelial dysfunction and atherosclerosis<sup>8</sup>. It has been suggested that EndMT promotes atherosclerosis through increased proatherogenic extracellular matrix component fibronectin, deposition, and expression of adhesion molecules<sup>9</sup>. However, the underlying molecular mechanism by which EndMT causes atherosclerosis remains unclear.

The Warburg effect, a phenomenon in which cancer cells predominantly rely on glycolysis to produce energy even under aerobic conditions, is a feature of metabolic reprogramming<sup>10</sup>. It

has been reported that the Warburg effect is involved in the progression of many diseases, like pulmonary arterial hypertension<sup>11</sup>, cardiac hypertrophy<sup>12</sup>, Parkinson's disease<sup>13</sup>, and cancer<sup>14</sup>. It is worth noting that ECs produce ATP mainly through aerobic glycolysis. Recent studies have found that aerobic glycolysis is increased in the ECs of atheroprone areas<sup>15</sup>. Elevated glycolysis increased the production of lactate, which could exacerbate cardiac fibrosis following myocardial infarction by disrupting endothelial cell function<sup>16</sup>, suggesting that endothelial dysfunction may be associated with the Warburg effect. Intriguingly, previous studies have shown that the Warburg effect is also involved in the EndMT in pulmonary arterial hypertension<sup>17</sup>. However, the impact of aerobic glycolysis on EndMT in atherosclerosis remains currently unknown.

Accumulating evidence demonstrated that CVDs are linked to epigenetic alterations, including DNA methylation, histone post-translational modifications, and non-coding RNAs<sup>18</sup>. There exists a variety of interplay between cellular dyshomeostasis and epigenetics. Our previous study has discovered that *S*-nitrosylated CTSB regulates its mRNA editing *via* an ADD1/MATR3/ADAR1 regulatory axis, leading to inflammasome activation and endothelial dysfunction, which may be a supplement to the classic "Central Dogma"<sup>19</sup>. However, the crosstalk between metabolic disturbances and epigenetic regulation during atherosclerosis is still unclear. Histones, a class of proteins that make up the nucleosome core around which DNA is wrapped, can influence chromatin accessibility in a variety of ways<sup>20</sup>. The tails of histones are constrained by several post-translational modifications, including methylation, acetylation, phosphorylation, glycosylation, SUMOylation, and ubiquitylation<sup>21</sup>. These post-translational histone modifications could dramatically regulate the chromatin architecture and gene expression by altering the chromatin microenvironment, playing a crucial role in the progression of many diseases<sup>22,23</sup>. Recently, histone lactylation was identified as

a novel function of glycolysis-derived lactate through the addition of lactyl groups to the lysine residues of histones<sup>24</sup>. Histone lactylation is closely associated with the initiation and development of various diseases, such as tumor<sup>25</sup>, Alzheimer's disease<sup>26</sup>, and pulmonary hypertension<sup>27</sup>. Previous studies have suggested that aortic bifurcations in patients with atherosclerosis are prone to endothelium damage because of hemodynamics, accompanied by increased glycolysis<sup>28</sup>. Therefore, it is intriguing to explore whether histone lactylation is involved in the development of atherosclerosis and to explain the underlying mechanism.

In this study, we reported that histone lactylation plays an essential role in the regulation of EndMT induced by lipid peroxidation. In the process, P300 and histone chaperone ASF1A (identified here as a key cofactor of P300 for the first time) cooperatively regulate histone H3 lysine 18 lactylation (H3K18la), which orchestrates the fine-tuning chromatin microenvironment surrounding *SNAIL* to increase its expression, inducing EndMT and atherosclerosis. Here, we illustrate a precise crosstalk between metabolism and epigenetics. Meanwhile, effective reduction of ASF1A expression by gene manipulation, inhibition of glycolysis by pharmacologic interference, and advanced PROTACs attenuated H3K18la, *SNAIL* transcription, and EndMT-induced atherosclerosis.

## 2. Materials and methods

### 2.1. Cell culture

Human coronary artery endothelial cells (HCAECs) were purchased from ScienCell and cultured in Endothelial Cell Medium (ScienCell) supplemented with 5% fetal bovine serum (FBS; ScienCell), 1% cell growth supplement, and 1% Penicillin/Streptomycin Solution (ScienCell). The HCAECs treated with human oxidized low-density lipoprotein (ox-LDL, 50  $\mu$ g/mL, 24 h; Yiyuan Biotechnologies) were used to establish an atherosclerotic endothelial injury. The HCAECs treated with phosphate buffer saline (PBS) were used as the control group. Mouse aortic endothelial cells (MAECs) were isolated from *ApoE*<sup>KO</sup>*Asf1a*<sup>WT</sup> and *ApoE*<sup>KO</sup>*Asf1a*<sup>ECKO</sup> mice and cultured in Dulbecco's modified Eagle's medium (DMEM) supplemented with 10% FBS and 1% penicillin/streptomycin solution. Cells were cultured in an incubator with 5% CO<sub>2</sub> at 37 °C in a humidified atmosphere.

### 2.2. Transfection

The transfection was performed using the Lipofectamine 3000 transfection reagent (Invitrogen) according to the manufacturer's protocol. Cells were seeded in culture dishes for 24 h. Small interfering RNA (siRNA; GenePharma) and the corresponding control RNA (siRNA NC) were transfected into cells at the logarithmic growth stage. Cells were transfected using siRNA and Lipofectamine 3000 transfection reagent at 70%–80% confluence, 48 h after transfection, other assays were performed. The sequence of siRNAs used is shown in [Supporting Information Table S1](#).

### 2.3. Microarray data and visualization

We obtained the microarray data from the Gene Expression Omnibus with the identification code GSE72633. The R package "pheatmap" (version 1.0.12) was used to visualize these data.

### 2.4. Measurement of lactate levels

Lactate levels were detected by the Lactate Colorimetric Assay Kit (Sigma–Aldrich), as described by the manufacturer. ECs were prepared using a lysis buffer. Lysates were sonicated on ice for 3 min and centrifuged at 4 °C for 10 min. We then collect the supernatant or prepared plasma samples to measure lactate levels. Briefly, lactate standards are diluted with lactate assay buffer and added to a 96-well plate, bringing the volume of lactate assay buffer to 50  $\mu$ L in each well, depending on the concentration of the dilution. The mixture was thoroughly mixed using a horizontal shaker or pipette, and the reaction was incubated for 30 min at room temperature, with the absorbance measured at the end.

### 2.5. Immunofluorescence

The cells were seeded in glass-bottom cell culture dishes. After different treatments, the cells were fixed with 4% paraformaldehyde, followed by permeabilization with 0.5% Triton X-100 (Invitrogen) for 20 min. Moreover, the heart with the proximal part of the ascending aorta was isolated and then embedded in an optimal cutting temperature compound (OCT; Servicebio). The aortas were snap-frozen at –80 °C and sliced into an 8  $\mu$ m frozen section. Frozen sections were oven dried at 55 °C for 15 min and then fixed in 4% paraformaldehyde for 20 min, followed by a drop of 0.1% Triton X-100 for 20 min to break the membrane. Subsequently, the samples were blocked with 10% BSA for 1 h and incubated with the specific primary antibodies at 4 °C overnight. The next day, the samples were washed with PBS and then incubated with secondary antibodies (Invitrogen) at 37 °C for 1 h. Finally, the nuclei were stained with 2-(4-amidinophenyl)-6-indolecarbamidine dihydrochloride (DAPI; Beyotime) at a ratio of 1:1000 for 10 min. The images were acquired using a confocal laser scanning microscope (Oberkoche).

### 2.6. Western blot assay

Cells and isolated arteries with different treatments were lysed with 1  $\times$  RIPA Lysis Buffer (Beyotime) and protease and phenylmethanesulfonyl fluoride (Beyotime) on ice for 30 min. The protein extract supernatant was collected after centrifugation at 4 °C (16,000  $\times$  g) for 20 min, and the protein concentration was determined using the BCA Protein Assay Kit (Beyotime). Denaturalized the supernatant in 1  $\times$  loading buffer at 95 °C for 10 min. Then, an equal amount of protein was separated on 10% sodium dodecyl sulfate-polyacrylamide gel electrophoresis and transferred to a PVDF membrane (Millipore). The membranes were blocked with 5% skim milk and subsequently incubated with primary antibodies at 4 °C overnight. After washing with TBST three times, the membranes were incubated with secondary antibodies at room temperature for 1 h. The bands were examined by Pierce ECL Western Blot Substrate, and the data were analyzed by ImageJ software. The antibodies used are shown in [Supporting Information Table S2](#).

### 2.7. Quantitative real-time PCR (RT-qPCR)

Total RNA was extracted from cultured cells using Trizol reagent (Invitrogen) following the manufacturer's instructions. The quality control of samples was carried out by Nanodrop™ One<sup>C</sup> (Thermo

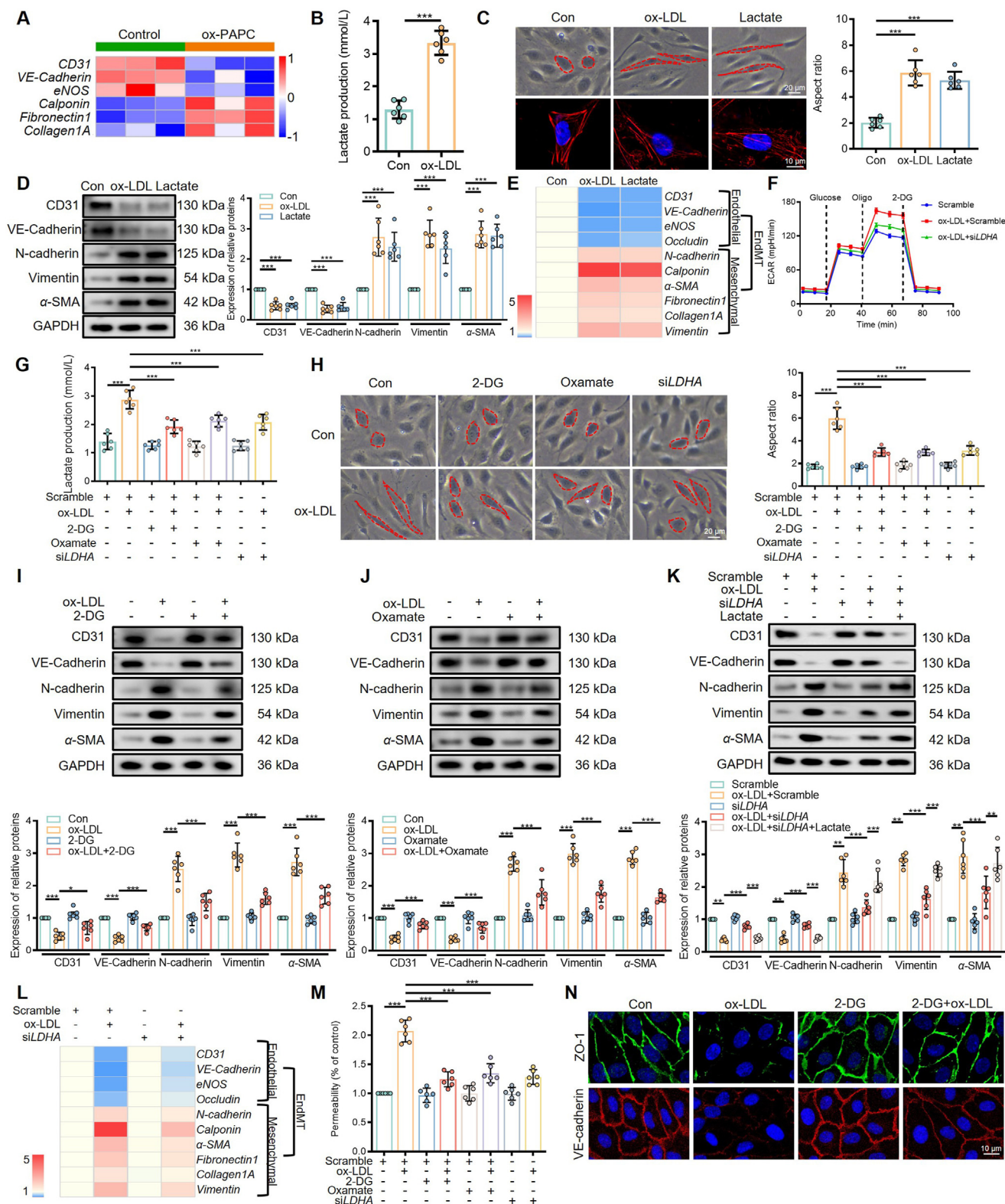


**Figure 1** Lipid peroxidation promotes EndMT by increasing lactate level. (A) Expression profiling by array assessing changes in endothelial cell markers in ox-PAPC-treated human aortic endothelial cells (GSE72633). The results are presented as a heat map, arranged from blue (low values) to red (high values). (B) Lactate levels in untreated and 50  $\mu$ g/mL ox-LDL-treated HCAECs for 24 h ( $n = 6$ ). (C) The morphology of HCAECs after ox-LDL and lactate treatment ( $n = 6$ ). (D) EC markers VE-cadherin and CD31, as well as EndMT markers  $\alpha$ -SMA, N-cadherin, and Vimentin, were detected in ox-LDL and lactate-treated ECs by Western blot ( $n = 6$ ). (E) RT-qPCR analysis of EndMT markers in ox-LDL and lactate-treated HCAECs ( $n = 6$ ). Each box color in the heat map corresponds to the average of the data from the corresponding 6 independent experiments. The column graphs with individual values and significance tests for each mRNA in the heat map are shown in Fig. S1A. (F) Real-

Fisher Scientific). Reverse transcription was carried out with HiScript-II-Q RT SuperMix (Vazyme). Then, RT-qPCR was performed on QuantStudio 5 Real-Time PCR system (Invitrogen) using AceQ qPCR SYBR Green Master Mix (Vazyme). All experiments were repeated three times. The levels of genes were normalized by the  $2^{-\Delta\Delta CT}$  method with GAPDH as references. The primers used in RT-qPCR are listed in [Supporting Information Table S3](#).

### 2.8. *In vitro* permeability assay

The FITC-dextran passage was quantitatively measured to estimate the degree of endothelial permeability. HCAECs were seeded at a density of  $10^5$  cells/mL on transwell membranes and grown to fusion to form a functional monolayer. Tracer Fluorescein isothiocyanate (FITC)-dextran (Sigma–Aldrich) with a final concentration of 1 mg/mL was added to the upper layer of the transwell chamber and incubated at 37 °C for 45 min. Samples were then collected from the upper and lower chambers, and the leakage of FITC-Dextran was evaluated. Fluorescence was measured (495 nm/519 nm) according to a standard curve on a plate reader (Molecular Devices). The permeability of the endothelial monolayer was evaluated as the permeability coefficient (Pd) using Eq. (1):

$$Pd = [A]/t \times 1/A \times V/[L] \quad (1)$$

where [A] is the concentration of dextran in the lower chamber,  $t$  is time in seconds,  $A$  indicates the membrane area in  $\text{cm}^2$ ,  $V$  is the lower chamber volume, and [L] is the dextran concentration in the upper chamber.

### 2.9. Animal

*Asf1a*<sup>fllox/fllox</sup> (*Asf1a*<sup>fl/fl</sup>) mice (strain No. T008410) were generated by GemPharmatech (Jiangsu, China) on a C57BL/6J background. Apolipoprotein E-knockout (*ApoE*<sup>KO</sup>) mice (strain No. T001458) were purchased from GemPharmatech (Jiangsu, China). *ApoE*<sup>KO</sup> *Asf1a* floxed (*ApoE*<sup>KO</sup>*Asf1a*<sup>fl/fl</sup>) mice were generated by crossbreeding *Asf1a*<sup>fl/fl</sup> mice with *ApoE*<sup>KO</sup> mice. Vascular endothelial-cadherin promoter-driven Cre recombinase line (*Cdh5-Cre*) mice were crossed with *ApoE*<sup>KO</sup> mice to generate *Cdh5-cre*<sup>+</sup>*ApoE*<sup>KO</sup> mice. *ApoE*<sup>KO</sup> endothelial-specific *Asf1a* knockout (*ApoE*<sup>KO</sup>*Asf1a*<sup>ECKO</sup>) mice were generated by crossbreeding *ApoE*<sup>KO</sup>*Asf1a*<sup>fl/fl</sup> mice with *Cdh5-cre*<sup>+</sup>*ApoE*<sup>KO</sup> mice. Littermate *ApoE*<sup>KO</sup>*Asf1a*<sup>WT</sup> (*ApoE*<sup>KO</sup>*Asf1a*<sup>fl/fl</sup>) mice were used as the control. The mice were housed in a temperature-controlled (22–25 °C) environment with a 12-h light/dark cycle in the Animal Center of Nanjing Medical University and had free access to water and food. To induce atherosclerosis, by 8 weeks of age, an equal number of

female and male mice were randomly assigned to the different experimental groups and given access to a normal chow (NC) or high-fat diet (HFD; 20% fat and 1.25% cholesterol; Xietong Organism Inc.) for 12 weeks. To investigate whether inhibiting glycolysis will impact atherosclerosis disease progression, we employed a competitive inhibitor of hexokinase 2-deoxy-glucose to examine the effect of glycolysis inhibition in the model of atherosclerosis using HFD-fed *ApoE*<sup>KO</sup> mice. Glycolysis inhibitor 2-deoxy-D-glucose (2-DG; Sigma–Aldrich) was added into the drinking water (0.2 mg/mL; *w/v*) of *ApoE*<sup>KO</sup> mice for 12 weeks, and mice were treated with 2-DG 50 mg/kg (1.25 mg per 6 mL; 6–7 mL/day), followed by pathological examination to determine whether pharmacological inhibition of histone lactylation offers any protection against atherosclerosis. To investigate the therapeutic effect of proteolysis-targeting chimera (PROTAC) hexokinase 2 (HK2) degrader-1 (MedChemExpress) on the atherosclerosis model established in *ApoE*<sup>KO</sup> mice under high-fat feeding, we randomly divided the mice into two groups and injected them intraperitoneally with PROTAC HK2 Degrader-1 (5 mg/kg) or Vehicle (PBS with an equal amount of DMSO) respectively, every other day for 12 weeks, and subsequently examined them to determine the PROTAC HK2 Degrader-1 efficacy. All procedures involving mice were in accordance with the Guide for the Care and Use of Laboratory Animals (NIH) and approved by the Animal Care and Use Committee of Nanjing Medical University. The mice were approved by the Animal Care and Use Committee of Nanjing Medical University (IACUC-2301005).

### 2.10. Isolation of mouse endothelial cells from aortas

Aortic endothelial cells were isolated and cultured as described, with some modifications<sup>29</sup>. Mice were anesthetized and then perfused with normal saline. The mouse aorta was exposed, and the aortic arch and thoracic aorta were isolated. We then carefully washed the tissue around the abdominal cavity and transferred the aortic arch and thoracic aorta to ice-cold PBS. After separation, the aorta was digested with collagenase to obtain ECs in preparation for Western blot or quickly rinsed using Trizol reagent, and the eluate was collected into 1.5 mL Eppendorf tubes and stored at –80 °C for RNA extraction.

### 2.11. Human samples

Human aorta samples with or without atherosclerosis were taken from grafts undergoing heart transplantation or coronary artery bypass grafting. All patients voluntarily provided written informed consent. All sampling procedures were authorized by The Ethics Committee of Nanjing Drum Tower Hospital, the Affiliated

time ECAR in control and ox-LDL cells with or without *siLDHA* treatment were measured at 20, 40, 60, 80, and 100 min by using the Seahorse Bioscience Extra Cellular Flux Analyzer ( $n = 6$ ). (G) Lactate levels in 2-DG, oxamate, and *siLDHA*-treated ECs ( $n = 6$ ). (H) The morphology of HCAECs after 2 mmol/L 2-DG, 10 mmol/L oxamate, and *siLDHA* treatment for 24 h ( $n = 6$ ). (I)–(K) ECs markers and EndMT markers were detected in 2-DG, oxamate and *siLDHA*-treated HCAECs by Western blot ( $n = 6$ ). (L) RT-qPCR analysis of EndMT markers in *siLDHA*-treated ECs ( $n = 6$ ). Each box color in the heat map corresponds to the average of the data from the corresponding 6 independent experiments. The column graphs with individual values and significance tests for each mRNA in the heat map are shown in [Fig. S1D](#). (M) Cell permeability of HCAECs after 2-DG, oxamate, and *siLDHA* treatment ( $n = 6$ ). (N) Cellular immunofluorescence analysis of ECs permeability after 2-DG treatment ( $n = 6$ ). (B) was analyzed by unpaired two-tailed student's  $t$ -test. (C)–(M) were analyzed by Ordinary one-way ANOVA with Tukey's multiple comparisons test. Data are shown as mean  $\pm$  SD; \*\* $P < 0.01$ , \*\*\* $P < 0.001$ . VE-cadherin: vascular endothelial cadherin; eNOS: endothelial nitric oxide synthases; HCAECs: human coronary artery endothelial cells; ox-LDL: oxidized low-density lipoprotein; ECAR: extracellular acidification rate; 2-DG: 2-deoxy-D-glucose; LDHA: lactate dehydrogenase A.

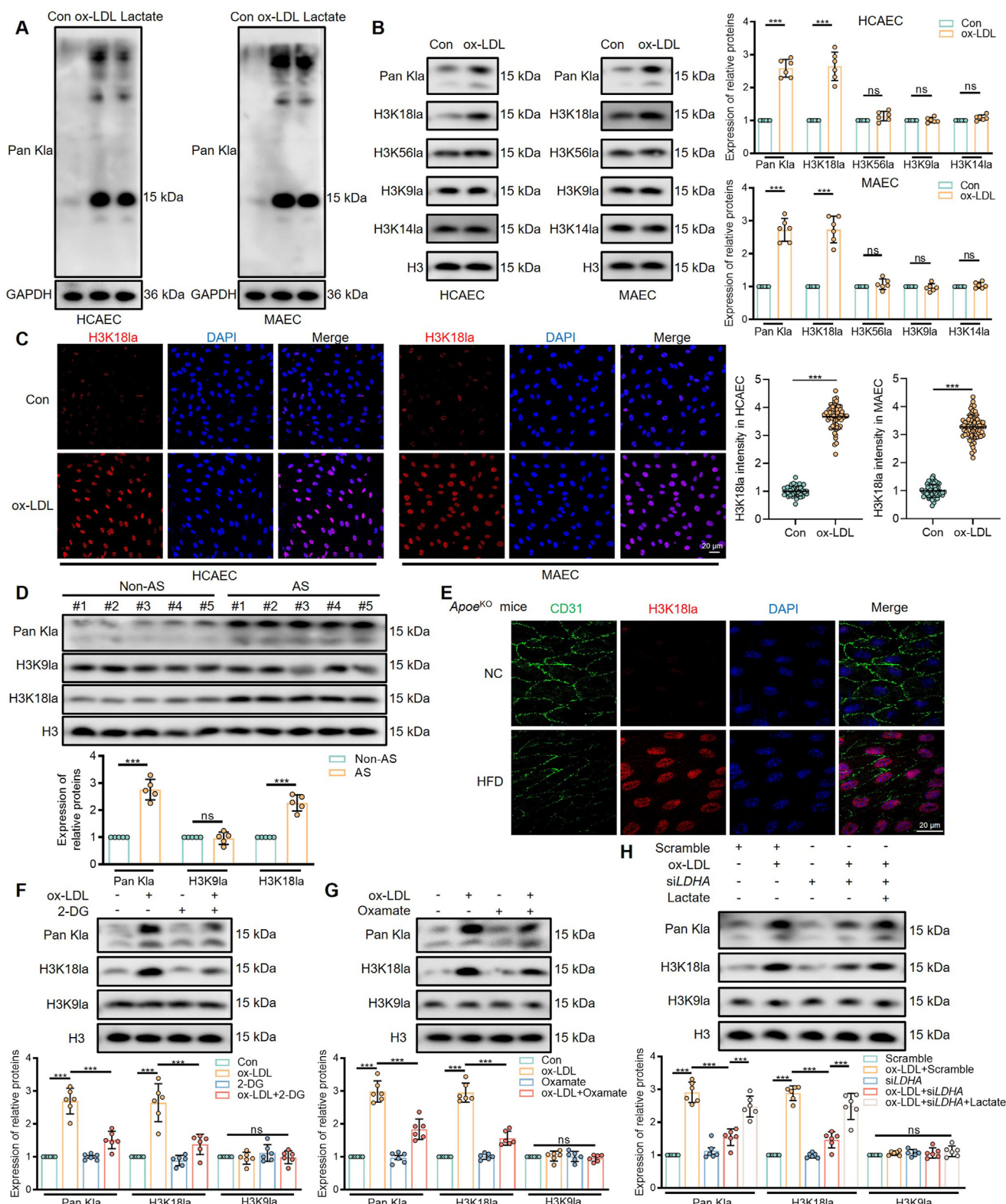


**Figure 2** Increased histone H3K18 lactylation is involved in endothelial dysfunction induced by lipid peroxidation. (A) Pan K1a was detected in ox-LDL and lactate-treated HCAECs and MAECs by Western blot ( $n = 6$ ). (B) Pan K1a, H3K18la, H3K56la, H3K9la, and H3K14la were detected in ox-LDL-treated HCAECs and MAECs by Western blot ( $n = 6$ ). (C) H3K18la levels were visualized by immunofluorescence staining ( $n = 6$ ). Scale bar, 20  $\mu$ m. (D) Pan K1a and H3K18la were detected in the aortic tissues from atherosclerotic patients or non-atherosclerotic patients by Western blot ( $n = 5$  human samples per group). (E) H3K18la levels were observed by enface staining of animal aortic tissues ( $n = 6$  mice per group). Scale bar, 20  $\mu$ m. (F)–(H) Pan K1a and H3K18la were detected in 2-DG, oxamate, and siLDHA-treated HCAECs by Western blot ( $n = 6$ ). (B)–(D) were analyzed by Unpaired *t*-test with Welch's correction. (F)–(H) were analyzed by Ordinary one-way ANOVA

Hospital of Nanjing University Medical School, and were performed according to the principles of the Declaration of Helsinki (2019-219-01). Detailed information is shown in [Supporting Information Table S4](#).

### 2.12. *En-face immunofluorescence staining*

En-face preparations were isolated from the thoracic aortas of different modelled mice. After being cleaned of excess tissue, the aorta vessels were rinsed in PBS in brief and fixed in 4% paraformaldehyde for 30 min. The vessels were then permeabilized with 0.1% Triton X-100 in PBS and blocked with 10% FBS in Tris-buffered saline (TBS) with 2.5% polysorbate 20 for 30 min at room temperature. Next, the aorta samples were incubated with 5 g/mL of indicated antibodies at 4 °C overnight in the blocking buffer. After rinsing the aorta samples with washing solution (TBS containing 2.5% polysorbate 20) 3 times, the fluorescence-conjugated secondary antibodies (1:200 dilution) were applied at room temperature for 1 h. Finally, the aorta samples were counterstained with DAPI (1 µg/mL) for 8 min and rinsed 3 × in the washing solution before being observed under a confocal laser scanning microscope (Oberkoche).

### 2.13. *Nuclear run-on assay*

To determine the rates of transcription in HCAECs, a nuclear run-on assay was performed according to the previously described protocol and the manufacturer's instructions<sup>30</sup>. Briefly, cell nuclei were collected *via* cold trypsinization on ice and added with 60 µL transcription buffer reaction cocktail master mix containing 1 × transcription buffer (10 mmol/L Tris-HCl, pH 8.3, 2.5 mmol/L MgCl<sub>2</sub>, 150 mmol/L KCl, and 2 mmol/L DTT), 100 U RNaseOUT, 0.5 mmol/L BrUTP, 1 mmol/L ATP, 1 mmol/L GTP, 1 mmol/L CTP and 0.5 mmol/L UTP. After transcription at 30 °C for 30 min, total nuclear RNA was isolated *via* the MEGAclear transcription clean-up kit (Invitrogen) following the manufacturer's instructions and subsequently quantified by NanoDrop. After immunoprecipitation of bromouridylated NRO-RNAs, NRO-RNAs were extracted using Trizol reagent (Invitrogen). Reverse transcription was performed, followed by RT-qPCR.

### 2.14. *Chromatin immunoprecipitation (ChIP) and Re-ChIP assay*

The ChIP assay was performed as previously described. HCAECs (3 × 10<sup>7</sup> cells per sample) were cross-linked with 1% formaldehyde for 20 min at room temperature and then quenched with ice-cold 0.125 mol/L glycine for 5 min. After washing with PBS, cells were collected and lysed in lysis buffer containing 1 × protease inhibitor cocktail II. Subsequently, the fraction was sonicated on ice to generate chromatin fragments ranging from 200 to 500 bp. After centrifugation at 4 °C for 10 min, 20 µL supernatant was collected as input, and the left was precleared in 20 µL protein A-agarose beads for 3 h at 4 °C, followed by incubation with antibodies overnight in continuous

rotation. After incubating with 40 µL protein A-agarose beads at 4 °C for 2 h, Txn stop buffer containing 0.4 mg/mL glycogen and 0.45 mg/mL proteinase K (Roche) was used for 1 h at room temperature, and then DNA was isolated and precipitated in ethanol. For the Re-ChIP assay, the chromatin samples from the primary immunoprecipitation were eluted with the elution buffer (1% SDS, 100 mmol/L NaHCO<sub>3</sub>), diluted in the Re-ChIP buffer (1% Triton X-100, 2 mmol/L EDTA, 150 mmol/L NaCl, 20 mmol/L Tris pH 8.1), and then subjected to a second immunoprecipitation using the indicated antibodies. After extensive washing and elution, the samples were then detected by RT-qPCR.

### 2.15. *ChIP-seq data and visualization*

The ChIP-seq data used in this study were available from the Gene Expression Omnibus with the identification codes GSE192358 and GSE171088. Data were visualized using the Integrative Genomics Viewer (Version: 2.8.10).

### 2.16. *Molecular docking model diagram*

This data is obtained *via* HDOCK (<http://hdock.phys.hust.edu.cn/>) and all parameters are selected by default. To ensure the comprehensiveness of the selected model, we chose model 8 and found out the functional residues used to form some hydrogen bond interactions, salt bridges, or hydrophobic interactions through LigPlot + 2.2.4, and used PyMol 2.2.0 to visualize the conformation of protein–protein docking. In LigPlot + 2.2.4, ASF1A is labeled as A, and p300 is labeled as B. In PyMol, ASF1A is represented as a blue-purple cartoon model, p300 is displayed as a blue cartoon model, and their junction points are displayed as a pink stick structure. When focusing on the binding region, the binding site will be displayed as the demonstration of the protein.

### 2.17. *Co-immunoprecipitation (co-IP)*

After treatment, HCAECs were harvested using cell lysis buffer with protease inhibitors and centrifuged to extract the supernatant for the co-IP assay. One-tenth of the supernatant was loaded as an input sample, and the remaining cell lysates were incubated with anti-IgG, anti-p300, and anti-ASF1A overnight at 4 °C with slow shaking. The next day, protein A/G agarose beads were added to the lysate and incubated for 4 h at 4 °C. They were then subjected to washing and eluted by boiling for 10 min in the loading buffer. Bead-bound proteins were analyzed by Western blot and immunoblotted with the indicated antibodies. IgG served as a negative control.

### 2.18. *In vitro lactylation assay*

The assay used recombinant histone H3.1-H4 tetramer (New England Biolabs) in a volume of 100 µL. For the assay in the absence or presence of ASF1A or ASF1A-V94R, mutants were added in molar equivalents to 0.25 µg of histone substrate in the assay

with Tukey's multiple comparisons test. Data are shown as mean ± SD; \**P* < 0.05, \*\**P* < 0.01, \*\*\**P* < 0.001; ns, not significant. Pan K1a: pan-lysine lactylation; H3K181a: histone H3 lysine 18 lactylation; MAECs: mouse aortic endothelial cells; AS: atherosclerosis; Apoe: apolipoprotein E; NC: normal chow; HFD: high-fat diet.

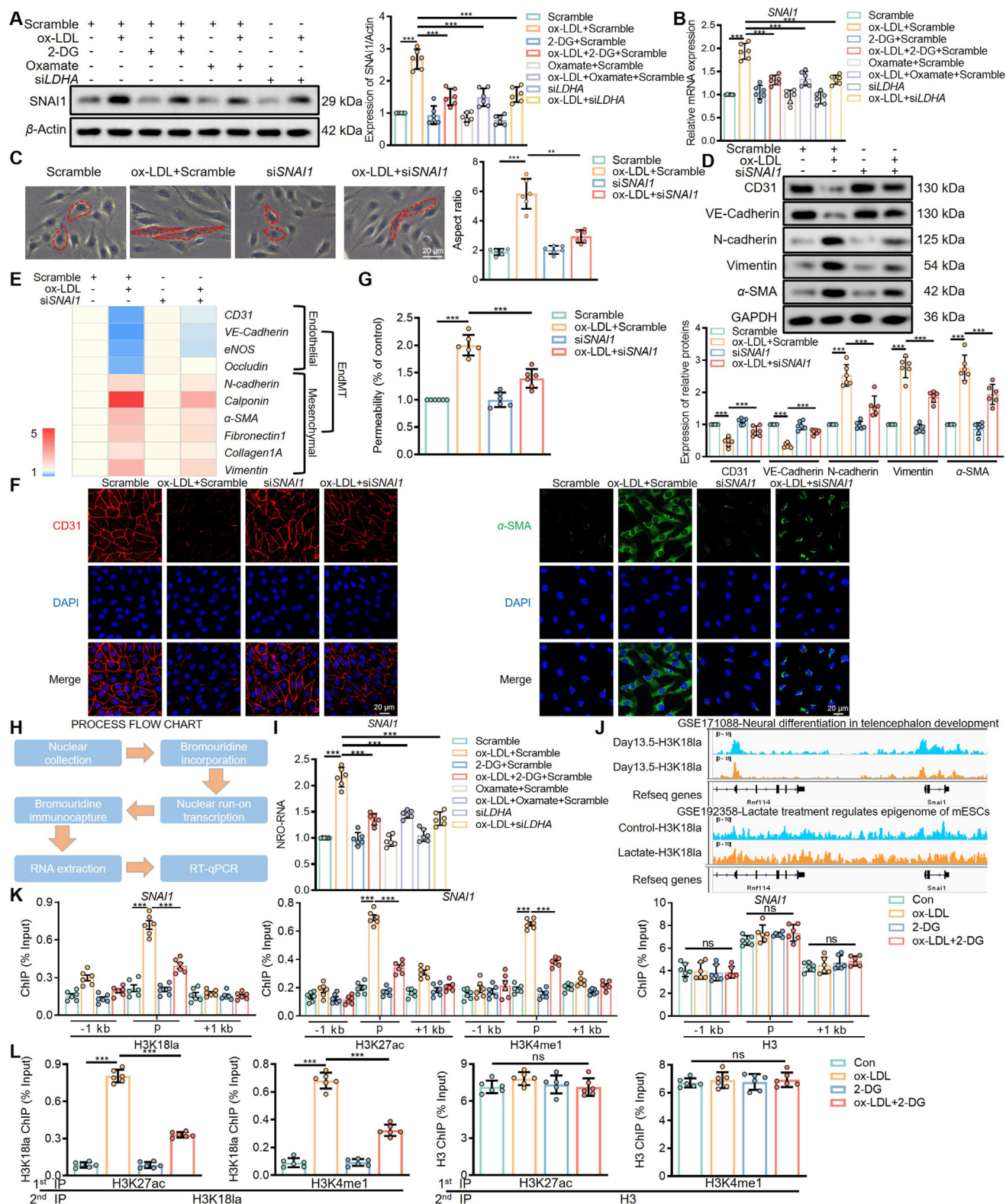


**Figure 3** Lipid peroxidation induces EndMT through H3K18la-enriched SNAI1. (A) SNAI1 was detected in 2-DG, oxamate, and siLDHA-treated HCAECs by Western blot ( $n = 6$ ). (B) RT-qPCR analysis of *SNAI1* in HCAECs ( $n = 6$ ). (C) The morphology of ox-LDL-treated HCAECs after interfering with *SNAI1* ( $n = 6$ ). (D) EndMT markers were detected in ox-LDL-treated HCAECs after interfering with *SNAI1* by Western blot ( $n = 6$ ). (E) RT-qPCR analysis of EndMT markers ( $n = 6$ ). Each box color in the heat map corresponds to the average of the data from the corresponding 6 independent experiments. The column graphs with individual values and significance tests for each mRNA in the heat map are shown in Fig. S2C. (F) CD31 and  $\alpha$ -SMA levels were visualized by immunofluorescence staining ( $n = 6$ ). Scale bar, 20  $\mu$ m. (G) Cell

buffer (50 mmol/L Tris-HCl, pH 8.0, 10% glycerol, 0.1 mmol/L EDTA, 1 mmol/L DTT, 1 mmol/L PMSF, 10 mmol/L sodium butyrate) in a 400  $\mu$ L total volume. To promote dissociation of the H3/H4 tetramers into H3/H4 dimers to enable ASF1 binding, the mixture was preincubated on ice for 10 min. L-Actyl-CoA was added to the reactions and incubated at 30 °C for 30 min. Finally, full-length p300 was added and incubated at 30 °C for 30 min. Reactions were precipitated using trichloroacetic acid and analyzed by Western blot assay.

### 2.19. Coomassie brilliant blue staining

According to the manufacturer's instructions, the gels were washed with deionized water after electrophoresis, the liquid was poured off, and 20 mL of Coomassie blue staining solution (Beyotime) was added and stained for 30 min. The staining solution was discarded, an appropriate amount of deionized water was added, and the gels were decolorized by shaking on a shaker. Every 30 min, replace with new deionized water. 2 h later, add another 100 mL of deionized water to decolorize the gel overnight and take photos for recording.

### 2.20. Chromatin conformation capture assay-qPCR (3C-qPCR)

With minor modifications, the 3C-qPCR assays were carried out as previously<sup>31</sup>. Briefly,  $1 \times 10^7$  HCAECs with different treatments were cross-linked with 1% formaldehyde for 20 min. After being quenched with glycine for 5 min at a final concentration of 125 mmol/L, cells were washed with ice-cold PBS twice and lysed with lysis buffer containing 10 mmol/L Tris-HCl pH 7.5, 10 mmol/L NaCl, 5 mmol/L MgCl<sub>2</sub>, 0.1 mmol/L EGTA, and 1  $\times$  complete protease inhibitor (Roche) on ice for 20 min, followed by centrifugation at 2500  $\times$  g for 5 min at 4 °C and digestion in 1.2  $\times$  restriction enzyme buffer with 0.3% SDS at 37 °C for 1 h with shaking at 100  $\times$  g. The pellets were then incubated with 0.2% Triton X-100 for 1 h at 37 °C and digested with 400 units of XbaI overnight at 37 °C. Nuclei were then incubated in 1.6% SDS at 65 °C for 25 min, then suspended and ligated in ligase buffer containing 1% Triton X-100 and 100 U ligase at 16 °C for 4 h, followed by room temperature for 30 min. 300  $\mu$ g Proteinase K buffer (5 mmol/L EDTA, pH 8.0; 10 mmol/L Tris-HCl, pH 8.0; 0.5% SDS) was applied to reverse crosslink at 65 °C overnight. DNA samples were then purified with RNase and extracted using the phenol-chloroform method, and then were used for qPCR analysis.

### 2.21. Assessment of aortic atherosclerotic lesion areas

Collagen content and tissue lipid accumulation were analyzed by hematoxylin and eosin (H&E) staining (Beyotime), Sirius red staining (Phygene), Masson staining (LEAGENE), and Oil Red O lipid staining (Sigma–Aldrich). Aortas were isolated from NC-fed

or HFD-fed mice, and hearts were excised. The sections were then encapsulated in OCT compound, cut crosswise into 8  $\mu$ m thick sections so that all three aortic valves were in the same geometric plane, and stained for Oil Red O according to the manufacturer's instructions. Frozen sections were fixed in 4% paraformaldehyde, ddH<sub>2</sub>O rinsed for 10 min, Oil Red O stock solution was filtered three times before being diluted to 60% working solution, and finally, the sections were immersed in Oil Red O working solution for immunostaining. H&E staining, Sirius red staining, and Masson trichrome staining were carried out according to the manufacturer's instructions. Images were captured using OLYMPUS BX53 (Olympus) and analyzed using Image-Pro Plus 6.0 software for the histological analysis of atherosclerotic lesions in the aortic root.

### 2.22. Seahorse extracellular flux assays

Cells were seeded onto Seahorse XF96 culture cell plates (Seahorse Bioscience) overnight ( $1.5 \times 10^4$  per well). The next day, the cells were washed with PBS and then fixed in an assay medium supplemented with glutamine. Subsequently, we added 10 mmol/L glucose, 1  $\mu$ mol/L oligomycin, and 50 mmol/L 2-DG to the cultured cells. After incubation in the medium in a non-CO<sub>2</sub> incubator at 37 °C for 1 h, cells were then measured using an XFe96 extracellular flux analyzer (Seahorse Bioscience) as previously described. Finally, we analyzed the extracellular acidification rate using Seahorse XF96 Wave software.

### 2.23. Blood lipid measurements

Assay kits for total cholesterol (T-CHO), low-density lipoprotein cholesterol (LDL-C), triglyceride (TG), and high-density lipoprotein cholesterol (HDL-C) were purchased from Nanjing Jiancheng Bioengineering Institute. Blood lipid measurements were performed according to the manufacturer's instructions. We extracted the tissues from mice and added 0.1 mol/L phosphate buffer solution (pH 7.4) or anhydrous ethanol. After centrifugation at 700  $\times$  g for 10 min on ice, the supernatant was taken for testing. The samples were incubated for 5 min at 37 °C and subsequently detected at 600 nm wavelengths.

### 2.24. Cell counting Kit-8 (CCK-8) assay

The cell viability of PROTAC HK2 Degrader-1 in HCAECs was assessed by the CCK-8 assay. Cells were seeded into 96-well plates at a density of  $6 \times 10^3$  per well, incubated at 5% CO<sub>2</sub>, 37 °C for 24 h, and then treated with different concentrations of PROTAC HK2 Degrader-1 for 48 h. Add 10  $\mu$ L of CCK-8 solution (Beyotime) to each well, and the incubation was continued for 2 h at 5% CO<sub>2</sub>, 37 °C. Absorbance was measured at 450 nm using a microplate reader.

permeability of ox-LDL-treated HCAECs after si*SNAI1* treatment ( $n = 6$ ). (H) Workflow chart for NRO, bromouridine immunocapture, and RT-qPCR. (I) Transcriptional regulation of *SNAI1* was analyzed by NRO assay ( $n = 6$ ). (J) ChIP-seq peaks around *SNAI1* from GSE171088 and GSE192358. (K) ChIP detection of binding sites of H3K181a at  $-1$  kb from the promoter, the promoter, and  $+1$  kb from the promoter region of *SNAI1*. ChIP detection of the degree of binding of control H3 to *SNAI1* ( $n = 6$ ). (L) Re-ChIP was performed with the first round including H3K27ac or H3K4me1 antibodies and a second round of pull-down with H3K181a antibodies ( $n = 6$ ). (A)–(E), (G), (I), (K), and (L) were analyzed by Ordinary one-way ANOVA with Tukey's multiple comparisons test. (C) was analyzed by Brown–Forsythe and Welch ANOVA followed by Dunnett's T3 multiple comparisons test. Data are shown as mean  $\pm$  SD; \*\* $P < 0.01$ , \*\*\* $P < 0.001$ . NRO: nuclear run-on; ChIP: chromatin Immunoprecipitation.

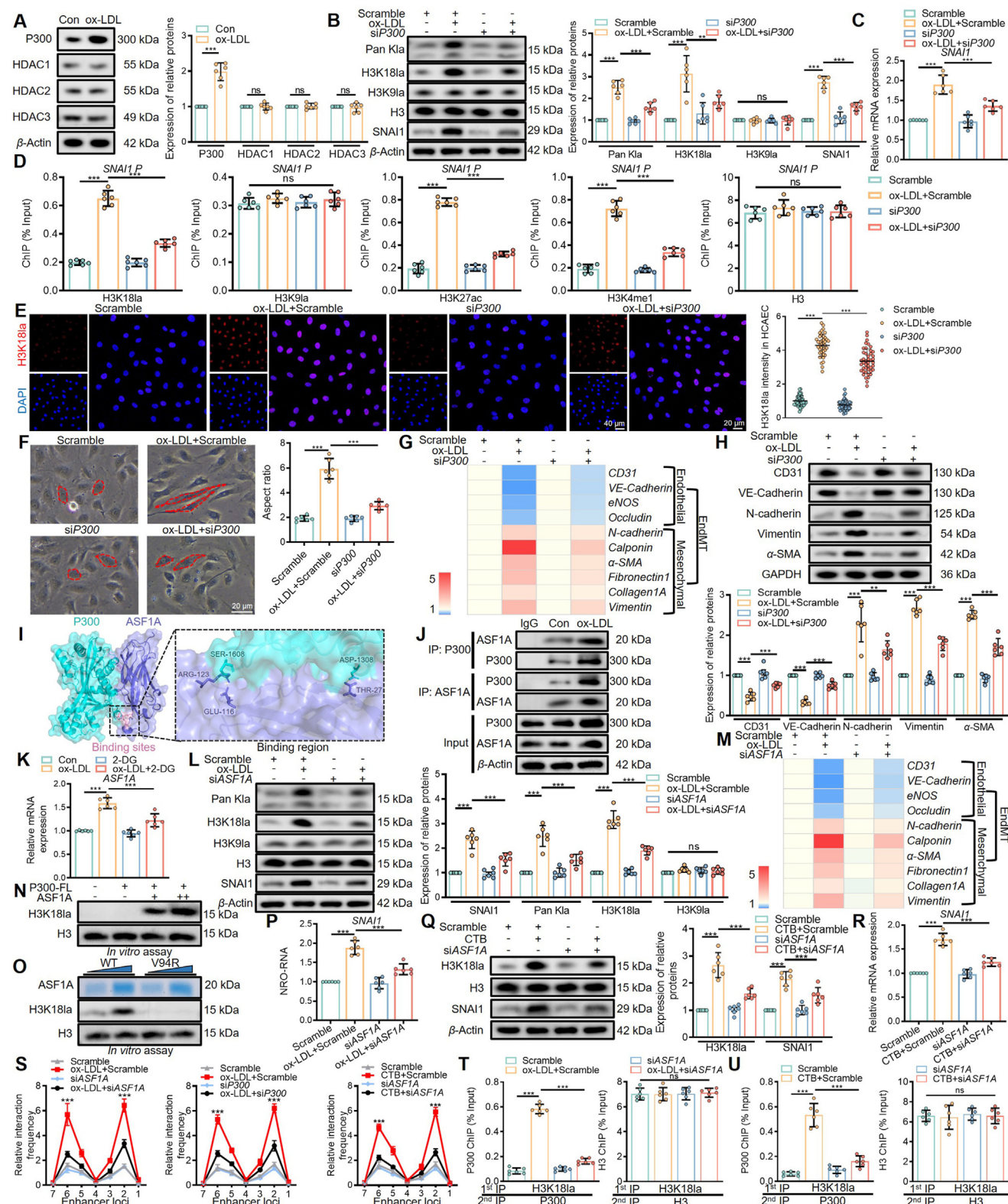


**Figure 4** The P300–ASF1A complex constitutes a chromosomal microenvironment to regulate the expression of *SNAI1* via H3K18la. (A) P300 and HDAC1–3 were detected in ox-LDL-treated HCAECs by Western blot ( $n = 6$ ). (B) Pan K1a, H3K18la, H3K9la, and SNAI1 levels were detected in ox-LDL-treated HCAECs after interfering with P300 by Western blot ( $n = 6$ ). (C) RT-qPCR analysis of *SNAI1* in ox-LDL-treated HCAECs after interfering with P300 ( $n = 6$ ). (D) ChIP analysis of the enrichment at the promoter of *SNAI1* ( $n = 6$ ). (E) H3K18la levels were visualized by immunofluorescence staining ( $n = 6$ ). Scale bar, 20  $\mu$ m. (F) The morphology of ox-LDL-treated HCAECs after interfering with P300 ( $n = 6$ ). (G) RT-qPCR analysis of endothelial mesenchymal transition markers in ox-LDL-treated HCAECs after interfering with P300 ( $n = 6$ ). Each box color in the heat map corresponds to the average of the data from the corresponding 6 independent experiments. The

### 2.25. Statistical analysis

Data are expressed as the mean value  $\pm$  the standard deviation (mean  $\pm$  SD). Data were statistically analyzed using GraphPad Prism 9.0 (GraphPad Software). Before performing parametric analyses, the Shapiro–Wilk test and Brown–Forsythe test were used to confirm normality and equal variance. Statistical significance was determined using the one-way analysis of variance (One-way ANOVA) with the Tukey *post hoc* test when there were three or more groups. Data that violated the equal variance assumption were handled with Brown–Forsythe and Welch ANOVA followed by Dunnett’s T3 multiple comparisons test. The unpaired student’s *t*-test with the assumption of equal variances was used to compare data from two groups. Data that violated the equal variance assumption were handled with Welch correction. Data that did not pass normality were analyzed using the Mann–Whitney U test. We used parametric tests since the data passed normality and equal variance tests. *P*-values  $<0.05$  was considered as statistical significance. Other materials are provided in Supporting Information Table S8.

## 3. Results

### 3.1. Lipid peroxidation promotes EndMT by increasing lactate level

As reported, oxidative PAPC stimulation can suppress the expression of endothelial cell-specific markers of human aortic endothelial cells, such as vascular endothelial cadherin (VE-cadherin), endothelial nitric oxide synthases (eNOS) and platelet endothelial cell adhesion molecule-1 (PECAM-1/CD31) and increase the expression of extracellular matrix proteins such as calponin, fibronectin 1, and collagen 1A in atherosclerotic patients (Fig. 1A), suggesting the EndMT process in endothelial dysfunction. Endothelial vulnerable areas in atherosclerotic patients exhibit active glycolysis<sup>15</sup>, which leads to elevated lactate levels, suggesting that lactate may be involved in regulating the process of EndMT. Therefore, we

examined the levels of lactate in HCAECs following ox-LDL stimulation and found a significant increase (Fig. 1B). Recent analyses of atherosclerosis markers and incident CVD events showed direct associations with lactate<sup>32</sup>. Therefore, we speculated whether ox-LDL-mediated EndMT occurred *via* lactate. We stimulated ECs with 50  $\mu\text{g}/\text{mL}$  ox-LDL and 10  $\text{mmol}/\text{L}$  lactate for 24 h, respectively. The ECs treated with ox-LDL or lactate underwent a morphological change from a cobblestone-like endothelial phenotype to a spindle-shaped mesenchymal phenotype (Fig. 1C). Both ox-LDL and lactate could decrease the protein and mRNA levels of EC markers, while increasing the levels of mesenchymal-specific markers such as N-cadherin,  $\alpha$ -SMA and Vimentin (Fig. 1D and E, and Supporting Information Fig. S1A). In contrast, the same treatment of non-oxidized forms of LDL had no obvious effect on the expression levels of EndMT markers, suggesting that LDL cannot induce EndMT in HCAECs as ox-LDL does (Fig. S1B). To further confirm the role of lactate in ox-LDL-mediated EndMT, we used small interfering RNA (siRNA) targeting lactate dehydrogenase A (*LDHA*) (Fig. S1C). The ox-LDL-induced extracellular acidification rate (ECAR) was significantly reduced after the *LDHA* deficiency by the seahorse analysis (Fig. 1F). The glycolysis inhibitor 2-DG, an inhibitor of hexokinase, and the lactate dehydrogenase inhibitor oxamate could also decrease the level of lactate in ECs induced by ox-LDL (Fig. 1G). Additionally, all of 2-DG, oxamate, and si*LDHA* could effectively inhibit the EndMT process induced by ox-LDL based on the morphological changes (Fig. 1H) and the protein and mRNA expression levels of EndMT-related genes (Fig. 1I–L, and Fig. S1D). Besides, adding lactate back into *LDHA*-deficient ECs correspondingly increased EndMT levels (Fig. 1K). The increase in endothelial cell permeability because of ox-LDL stimulation was also inhibited by 2-DG, oxamate, and si*LDHA* (Fig. 1M). Cellular immunofluorescence further confirmed this by a decrease in the tight junction proteins zona occludens 1 (*ZO-1*) and VE-cadherin in ox-LDL-treated cells, which was restored by 2-DG (Fig. 1N). These data indicated that ox-LDL can induce EndMT by increasing lactate production, which leads to an increase in the endothelial permeability and consequently to the development of atherosclerosis.

column graphs with individual values and significance tests for each mRNA in the heat map are shown in Fig. S3B. (H) Endothelial-like cell markers VE-Cadherin and CD31, as well as mesenchymal-like cells  $\alpha$ -SMA and Vimentin were detected in ox-LDL-treated HCAECs after interfering with P300 by Western blot ( $n = 6$ ). (I) Molecular docking diagram (<http://hdock.phys.hust.edu.cn/>) of ASF1A and P300. (J) Co-immunoprecipitation analysis of ASF1A-P300 binding in ox-LDL-treated HCAECs ( $n = 6$ ). (K) RT-qPCR analysis of *ASF1A* expression in ox-LDL and 2-DG-treated ECs ( $n = 6$ ). (L) Pan K1a, H3K181a, H3K91a, and SNAI1 were detected in ox-LDL and siASF1A-treated HCAECs by Western blot ( $n = 6$ ). (M) RT-qPCR analysis of endothelial mesenchymal transition markers in ox-LDL-treated HCAECs after interfering with *ASF1A* ( $n = 6$ ). Each box color in the heat map corresponds to the average of the data from the corresponding 6 independent experiments. The column graphs with individual values and significance tests for each mRNA in the heat map are shown in Fig. S3E. (N) *In vitro* assays to monitor H3K18 lactylation with H3–H4 substrates in the presence of full-length P300 (P300-FL) in the presence or absence of ASF1A ( $n = 6$ ). (O) *In vitro*, assays were performed with P300 in the presence of increasing concentrations of wild-type (WT) ASF1A or ASF1A-V94R mutant (defective in interaction with histones). ASF1A proteins are shown by Coomassie brilliant blue staining. H3K181a was detected by Western blot ( $n = 6$ ). (P) The transcription of *SNAI1* in HCAECs treated with ox-LDL or siASF1A was analyzed by NRO-RNAs ( $n = 6$ ). (Q) H3K181a and SNAI1 were detected in CTB and siASF1A-treated HCAECs by Western blot ( $n = 6$ ). (R) RT-qPCR analysis of *SNAI1* expression in CTB-treated HCAECs after interfering with *ASF1A* ( $n = 6$ ). (S) 3C-qPCR analysis of long-range interactions between the *SNAI1* promoter and seven binding sites in ox-LDL-treated HCAECs combined with the deficiency of *ASF1A* or *P300* and CTB-treated HCAECs after interfering with *ASF1A* ( $n = 6$ ). (T) Re-ChIP was performed with the first round with H3K181a antibody and a second round of pull-down with P300 antibodies in HCAECs treated with ox-LDL or siASF1A ( $n = 6$ ). (U) Re-ChIP was performed with the first round with H3K181a antibody and a second round of pull-down with P300 antibodies in HCAECs treated with CTB or siASF1A ( $n = 6$ ). (A) was analyzed by unpaired *t*-test with Welch’s correction. (B)–(D), (G) and (H), (K)–(M), (P)–(R), and (T) were analyzed by Ordinary one-way ANOVA with Tukey’s multiple comparisons test. (E), (F) and (U) were analyzed by Brown–Forsythe and Welch ANOVA followed by Dunnett’s T3 multiple comparisons test. (S) was analyzed by Two-way ANOVA followed by a *post hoc* test. Data are shown as mean  $\pm$  SD; \* $P < 0.05$ , \*\* $P < 0.01$ , \*\*\* $P < 0.001$ ; ns, not significant. HDAC: histone deacetylase; 3C-qPCR: chromatin conformation capture assay-qPCR; ASF1A: anti-silencing function 1A; CTB: cholera toxin B.

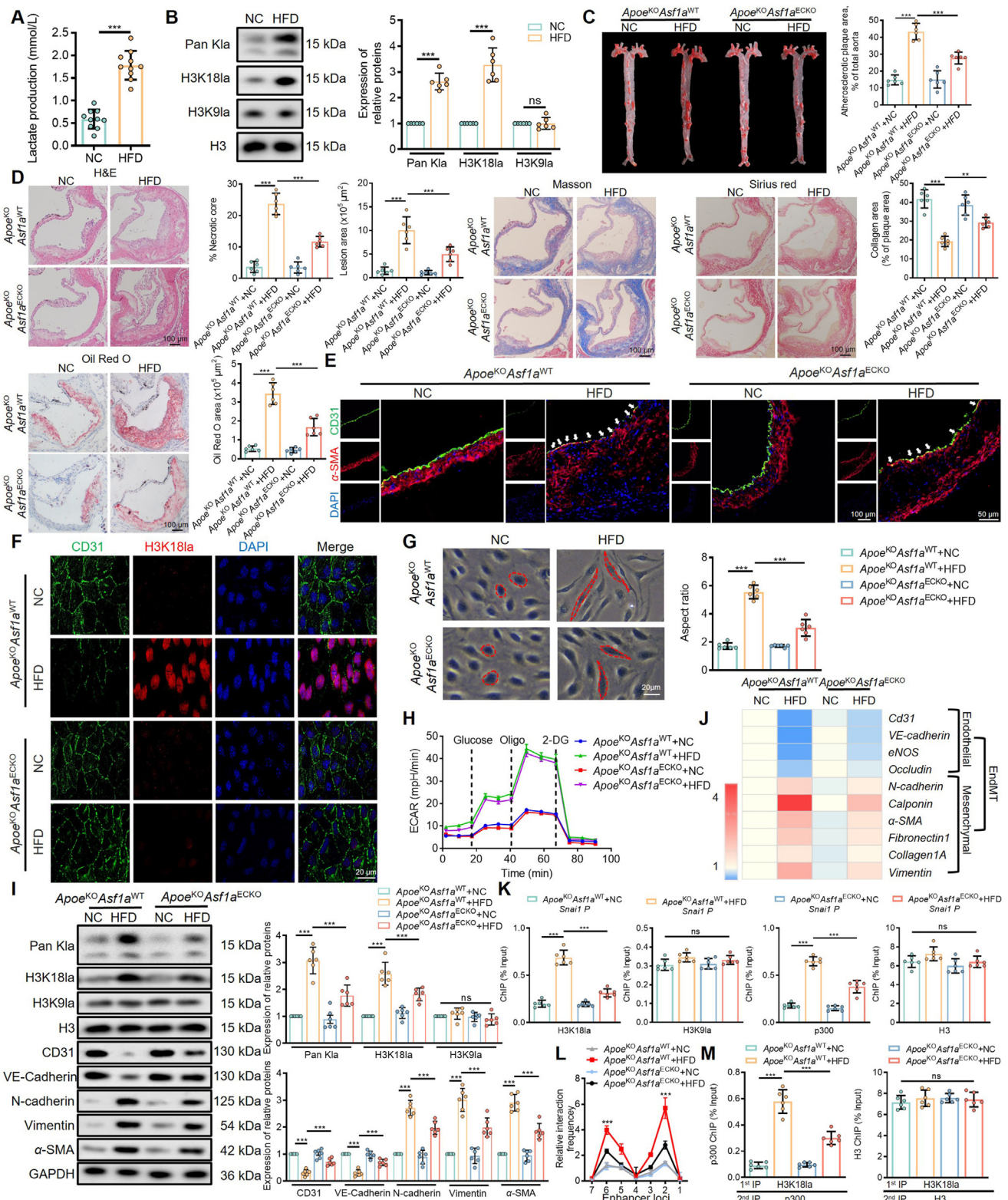


**Figure 5** *Asf1a*-specific deletion in ECs ameliorates EndMT and atherosclerosis in *Apoe*<sup>KO</sup> mice. (A) Blood lactate levels in NC-fed and HFD-fed *Apoe*<sup>KO</sup> mice ( $n = 10$  mice per group). (B) Pan K1a, H3K91a, and H3K181a were detected in NC-fed and HFD-fed *Apoe*<sup>KO</sup> mice by Western blot ( $n = 6$  mice per group). (C) Representative images of aortas stained with Oil Red O from *Apoe*<sup>KO</sup>*Asf1a*<sup>WT</sup> and *Apoe*<sup>KO</sup>*Asf1a*<sup>EKO</sup> mice fed with an NC or HFD. The quantitative data of Oil Red O staining of mouse blood vessels ( $n = 6$  mice per group). (D) Atherosclerotic lesion formation was detected by H&E, Oil Red O, Sirius red, and Masson's trichrome staining ( $n = 6$  mice per group). Scale bar, 100  $\mu$ m. Quantification of lesions area and Oil Red O area. Percentage of necrotic core and collagen area. (E) Confocal microscopic image of double immunofluorescence staining with CD31 (green) and  $\alpha$ -SMA (red); nuclei were counter-stained with DAPI (blue) ( $n = 6$  mice per group). Scale bars,

### 3.2. Increased histone H3K18 lactylation is involved in endothelial dysfunction induced by lipid peroxidation

It has been reported that lactate can increase histone lactylation and change gene expression<sup>24</sup>. Based on the above, we speculated that the increased lactate in ox-LDL-treated ECs could alter histone lactylation. Western blot analysis showed that both HCAECs and MAECs showed significantly higher levels of total protein lactylation than normal ECs after being treated with ox-LDL or lactate, and the major band of protein lactylation was around 15 kDa, presumably histone H3, so we speculated that histone might be the lactylation target (Fig. 2A). Further, Western blot analysis showed the same trend in the levels of Pan-lysine lactylation (Pan K1a) and H3K181a in both ox-LDL-treated HCAECs and MAECs, with barely any change in other histones such as histone H3 lysine 56 lactylation (H3K561a), histone H3 lysine 9 lactylation (H3K91a), and histone H3 lysine 14 lactylation (H3K141a) (Fig. 2B). Immunofluorescence staining suggested that H3K181a was mainly localized in the nucleus and significantly increased in response to ox-LDL stimulation (Fig. 2C). Similarly, the expression levels of Pan K1a and H3K181a were increased in the aortic tissues of atherosclerotic patients (Fig. 2D, and Table S4). In addition, enface staining results from animal aortic tissues also showed that H3K181a was significantly increased in high-fat diet (HFD)-fed apolipoprotein E-knockout (*ApoE*<sup>KO</sup>) mice (Fig. 2E). To further demonstrate that ox-LDL increases histone lysine lactylation *via* lactate, we reduced overall intracellular histone lactylation levels in HCAECs by reducing lactate production using the glycolysis inhibitor 2-DG, the lactate dehydrogenase inhibitor oxamate, and siRNA for *LDHA*. As expected, all three were able to significantly reduce global intracellular lactylation and H3K181a levels in ox-LDL-treated ECs (Fig. 2F–H). Collectively, these data suggest that ox-LDL stimulation promotes H3K181a expression in ECs by increasing lactate production.

### 3.3. Lipid peroxidation induces EndMT through H3K181a-enriched *SNAIL*

During EMT and EndMT, *SNAIL* is an essential transcription factor<sup>33</sup>. It has been shown that lactate dose-dependently increases *SNAIL* expression and induces EMT in lung cancer cells<sup>34</sup>. In our study, the protein and mRNA expression of *SNAIL* but not *SLUG*, *TWIST1*, and *ZEB1* was significantly increased in ox-LDL-treated ECs (Supporting Information Fig. S2A), and the expression of

*SNAIL* was reversed by 2-DG, oxamate, and si*LDHA* (Fig. 3A and B). This suggests that lactate may promote EndMT through the transcriptional regulation of *SNAIL*. Interfering with *SNAIL* could significantly inhibit the morphological change of ECs induced by ox-LDL (Fig. 3C and Fig. S2B) and effectively reverse the decreased expression of endothelial gene markers and increase the expression of mesenchymal gene expression in ox-LDL-treated ECs (Fig. 3D–F, and Fig. S2C). In addition, interfering with *SNAIL* inhibited the increase in endothelial cell permeability caused by ox-LDL (Fig. 3G). The above experimental results suggest that ox-LDL can upregulate the expression of *SNAIL* in ECs by increasing lactate production, thereby leading to EndMT. Our previous findings have demonstrated that ox-LDL stimulation promotes H3K181a in ECs by increasing lactate production (Fig. 2), so we speculate that lactate can regulate *SNAIL* expression and promote EndMT by increasing H3K181a. To explore how histone lactylation contributes to the EndMT phenotype, we used a highly optimized and validated nuclear run-on (NRO) assay based on bromelain immunocapture and RT-qPCR to investigate the transcriptional regulation of the *SNAIL* promoter (transcriptional start sites) (Fig. 3H). We found that transcriptional activity on the *SNAIL* promoter was significantly elevated following ox-LDL treatment, which was reversed by glycolysis inhibitors and lactate dehydrogenase inhibitors (Fig. 3I). The corresponding ChIP-seq data from lactate-stimulated embryonic stem cells and mouse telencephalon development were displayed using the Integrative Journal Pre-proof Genomics Viewer. ChIP-seq results showed the enrichment of H3K181a at the *SNAIL* promoter (Fig. 3J). We examined the expression level of H3K181a at the *SNAIL* promoter and found that H3K181a and active histone markers histone H3 Lysine 27 acetylation (H3K27ac) and histone H3 lysine 14 lactylation (H3K4me1) were enriched in the *SNAIL* promoter region after ox-LDL treatment, and this enrichment was repressed by 2-DG (Fig. 3K). Re-ChIP analysis further confirmed that H3K181a was enriched at active enhancers that were near the *SNAIL* promoter (Fig. 3L). The above results suggest that ox-LDL affects the gene expression of *SNAIL* by increasing H3K181a, which in turn induces EndMT.

### 3.4. The P300–ASF1A complex constitutes a chromosomal microenvironment to regulate the expression of *SNAIL* via H3K181a

Multiple studies have reported that histone acetyltransferase P300 is an indicative histone lactylation writer protein and that histone

50  $\mu$ m. (F) Confocal microscopic image of double immunofluorescence staining with CD31 (green) and H3K181a (red); nuclei were counterstained with DAPI (blue) ( $n = 6$  mice per group). Scale bars, 20  $\mu$ m. (G) The morphology of MAECs extracted from the aorta of *ApoE*<sup>KO</sup>*Asf1a*<sup>WT</sup> and *ApoE*<sup>KO</sup>*Asf1a*<sup>ECKO</sup> mice fed with an NC or HFD ( $n = 6$  mice per group). (H) ECAR of NC-fed and HFD-fed *ApoE*<sup>KO</sup>*Asf1a*<sup>ECKO</sup> mice were monitored by using the Seahorse Bioscience Extra Cellular Flux Analyzer in real-time. Real-time ECAR was measured at 20, 40, 60, 80, and 100 min ( $n = 6$  mice per group). (I) Pan K1a, H3K181a, H3K91a, VE-Cadherin, CD31, N-cadherin,  $\alpha$ -SMA, and Vimentin levels were detected in MAECs extracted from *ApoE*<sup>KO</sup>*Asf1a*<sup>WT</sup> and *ApoE*<sup>KO</sup>*Asf1a*<sup>ECKO</sup> mice by Western blot ( $n = 6$  mice per group). (J) RT-qPCR analysis of EndMT markers in NC-fed and HFD-fed *ApoE*<sup>KO</sup>*Asf1a*<sup>ECKO</sup> mice ( $n = 10$  mice per group). Each box color in the heat map corresponds to the average of the data from the corresponding 10 independent experiments. The column graphs with individual values and significance tests for each mRNA in the heat map are shown in Fig. S4D. (K) ChIP analysis of the enrichment of P300 and H3K181a at the promoter region of *Snail* in MAECs extracted from *ApoE*<sup>KO</sup>*Asf1a*<sup>WT</sup> and *ApoE*<sup>KO</sup>*Asf1a*<sup>ECKO</sup> mice ( $n = 6$  mice per group). (L) 3C-qPCR analysis of long-distance interactions between the *Snail* promoter region and seven loci in MAECs extracted from *ApoE*<sup>KO</sup>*Asf1a*<sup>WT</sup> and *ApoE*<sup>KO</sup>*Asf1a*<sup>ECKO</sup> mice ( $n = 6$  mice per group). (M) Re-ChIP was performed with the first round with H3K181a antibody and a second round of pull-down with P300 antibody in MAECs extracted from *ApoE*<sup>KO</sup>*Asf1a*<sup>WT</sup> and *ApoE*<sup>KO</sup>*Asf1a*<sup>ECKO</sup> mice ( $n = 6$  mice per group). (A) was analyzed by unpaired two-tailed student's *t*-test. (B) was analyzed by unpaired *t*-test with Welch's correction. (C) and (D), (G), (I)–(K), and (M) were analyzed by Ordinary one-way ANOVA with Tukey's multiple comparisons test. (L) was analyzed by Two-way ANOVA followed by a *post hoc* test. Data are shown as mean  $\pm$  SD; \*\* $P < 0.01$ , \*\*\* $P < 0.001$ ; ns, not significant. H&E: hematoxylin & eosin.

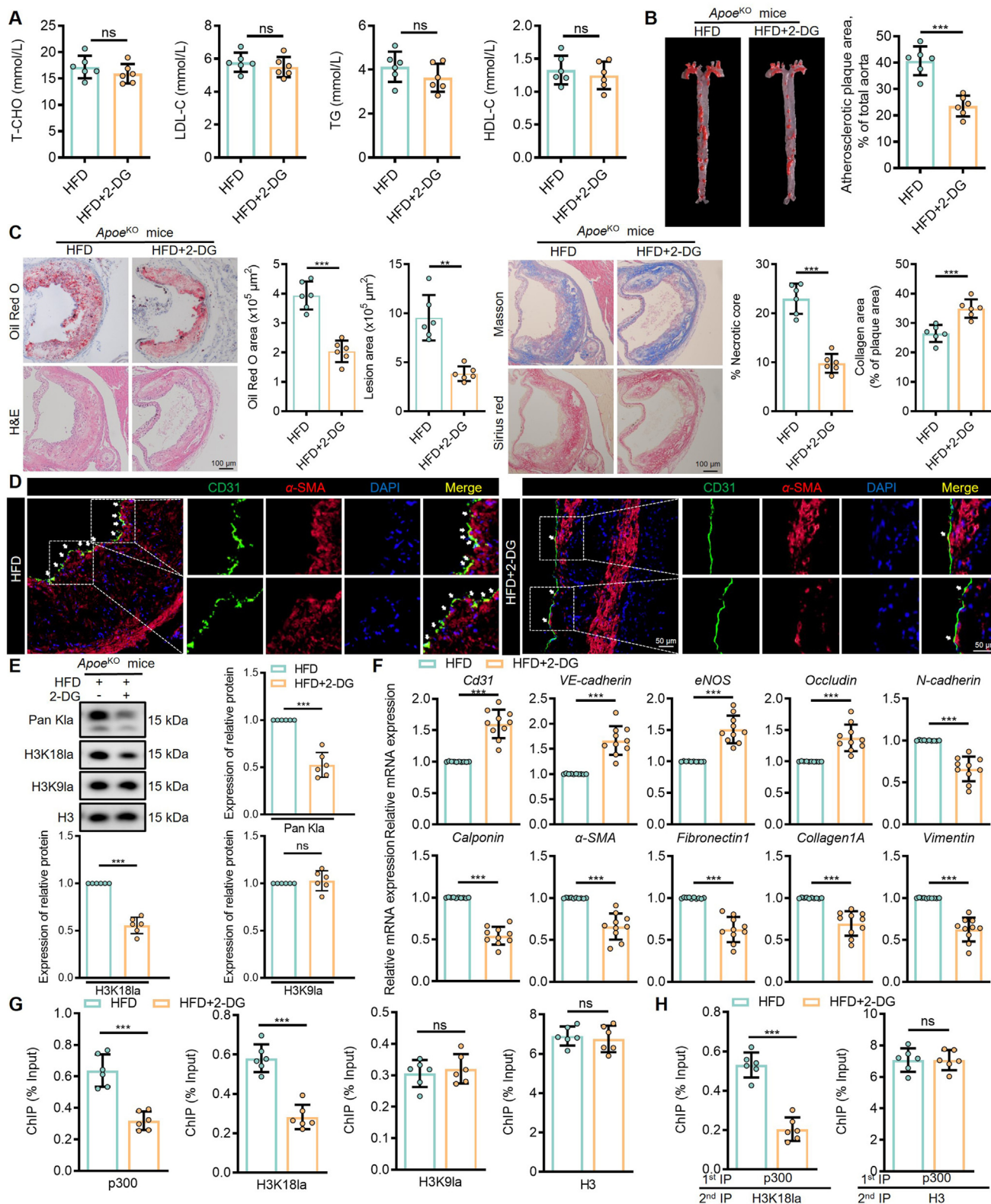


**Figure 6** Pharmacological inhibition of lactate levels reduces EndMT and atherosclerosis in *Apoe*<sup>KO</sup> mice. (A) The plasma levels of T-CHO, LDL-C, TG, and HDL-C levels in HFD-fed *Apoe*<sup>KO</sup> mice fed with or without 2-DG (50 mg/kg, q.d. for 12 weeks) measured by corresponding kits ( $n = 6$  mice per group). (B) Representative images of aortas stained with Oil Red O from HFD-fed *Apoe*<sup>KO</sup> mice fed with or without 2-DG. The quantitative data of Oil Red O staining of mouse blood vessels ( $n = 6$  mice per group). (C) Atherosclerotic lesion formation detected by H&E, Oil Red O, Sirius red, and Masson's trichrome staining ( $n = 6$  mice per group). Scale bar, 100  $\mu\text{m}$ . Quantification of lesions area and Oil Red O area. Percentage of necrotic core and collagen area. (D) Confocal microscopy images of mouse blood vessel cross-sections double immunofluorescence

deacetylase (HDAC) 1–3 are the main cellular “eraser” proteins<sup>24,35</sup>. To investigate the mechanism of increased histone lactylation by ox-LDL, we measured the expression levels of P300 and HDAC1–3 in ox-LDL-treated ECs. The expression of P300 increased significantly in ox-LDL-treated ECs (Fig. 4A). Interference with *P300* (Supporting Information Fig. S3A) could significantly decrease the levels of both Pan K1a, H3K181a, and *SNAI1* in ox-LDL-treated ECs (Fig. 4B and C). Additionally, we observed that H3K181a was enriched in the *SNAI1* promoter region, which was reversed by interfering with *P300* (Fig. 4D). Deficiency of *P300* can decrease the expression level of H3K181a, inhibit ECs from undergoing morphological changes (Fig. 4E and F), and diminish the occurrence of EndMT (Fig. 4G, H, and Fig. S3B). Taken together, these data suggest that P300 is associated with histone lactylation and contributes to EndMT phenotypic changes.

According to previous literature, Anti-silencing function 1A (ASF1A), nucleosome assembly protein 1 (NAP1), nucleophosmin 1 (NPM1), RB binding protein 7 (RBAP46), and RB binding protein 4 (RBAP48) are histone chaperones that bind to P300<sup>36–39</sup>. Co-immunoprecipitation results show the binding of histone H3/H4 chaperones ASF1A and P300 could be significantly enhanced under ox-LDL stimulation (Fig. S3C). ASF1A is an evolutionarily well-conserved histone H3/H4 chaperone and a crucial regulator of gene transcription<sup>40</sup>. It has been reported that ASF1A can interact with P300 to form complexes that regulate histone modification<sup>39</sup>. Molecular docking of ASF1A and P300 by Dockeasy revealed that the two proteins could be docked to each other. There are multiple groups of residues used to form hydrogen bonds between ASF1A and P300, such as the hydrogen bond formed by Glu-116 of ASF1A and Ser-1608 of P300 (Fig. 4I). The above results suggest whether ASF1A can act together with P300 to regulate the transcriptional activity of *SNAI1*. Co-immunoprecipitation results showed that the interaction between ASF1A and P300 was enhanced by ox-LDL treatment (Fig. 4J). Meanwhile, the mRNA level of *ASF1A* was increased under ox-LDL treatment, which was reversed by lactate deficiency, indicating that ox-LDL could promote *ASF1A* expression by increasing lactate (Fig. 4K). Besides, *ASF1A* deficiency (Fig. S3D) significantly inhibited the increase of H3K181a and *SNAI1* levels induced by ox-LDL, as well as the EndMT process (Fig. 4L and M, and Fig. S3E). Given that the interference of *ASF1A* reduced P300-mediated lactylation of H3K181a in HCAECs, we further explored whether ASF1A was also involved in P300-mediated lactylation *in vitro*. The assays were performed under conditions of restricted amounts of P300 and conditions favoring H3–H4 dimer, *i.e.*, H3–H4 tetramer equilibrium tilted to the H3–H4 dimer state. In addition, we preincubated histones with ASF1A to promote the formation of ASF1A–H3–H4 dimer complexes. The results showed that ASF1A dose-dependently enhanced the lactylation of H3K18 *in vitro* (Fig. 4N and

Fig. S3F). We next investigated whether the interaction between ASF1A and histones is required for ASF1A to participate in P300-mediated lactylation of H3K18. Previous studies demonstrated that the V94R mutation of ASF1A disrupts the ability of ASF1A to bind to histones<sup>41</sup>. Our results showed that the V94R mutant version of ASF1A fails to assist P300-mediated lactylation of H3K18, suggesting that ASF1–H3–H4 interaction is essential for P300-mediated H3K18 lactylation on free histones (Fig. 4O and Fig. S3G). Since P300 was found to regulate the transcriptional activity of *SNAI1* in this study and there was a correlation between P300 and ASF1A, we observed a significant reduction in *SNAI1* transcription after interference with *ASF1A* by NRO assay (Fig. 4P). P300 agonist cholera toxin B (CTB) elevated H3K181a and *SNAI1*, which was reversed by *ASF1A* deficiency (Fig. 4Q and R). To confirm the interaction between the promoters of *SNAI1* and these potential active loci, we performed a quantitative analysis of 3C-qPCR. As shown in Fig. 4S, interfering with *ASF1A* or *P300* could significantly inhibit the chromosome interaction in the *SNAI1* promoter region induced by ox-LDL or CTB. Re-ChIP analysis also showed that H3K181a and P300 bind to the same promoter region of the *SNAI1* gene in ox-LDL-treated or CTB-treated HCAECs, while the binding decreased with the interference of *ASF1A* (Fig. 4T and U). Therefore, we conclude that P300, H3K181a, and ASF1A constitute a chromosomal microenvironment where the P300/ASF1A molecular complex could precisely regulate the enrichment of H3K181a at the promoter of *SNAI1*, regulating the expression of *SNAI1*, and thus influencing EndMT.

### 3.5. *Asf1a*-specific deletion in ECs ameliorates EndMT and atherosclerosis in *Apoe*<sup>KO</sup> mice

To confirm the role of histone lactylation on endothelial dysfunction and atherosclerosis, we detected lactate levels, which were significantly increased in the plasma of HFD-fed *Apoe*<sup>KO</sup> mice (Fig. 5A). Meanwhile, there is a significant increase in the expression of Pan K1a and H3K181a levels in HFD-fed *Apoe*<sup>KO</sup> mice (Fig. 5B). Then, we achieved mice with specific deletion of *Asf1a* in ECs (*Apoe*<sup>KO</sup>*Asf1a*<sup>ECKO</sup>) by crossing *Asf1a* floxed (*Asf1a*<sup>fl/fl</sup>) mice with a vascular endothelial-cadherin promoter-driven Cre recombinase line (Cdh5-Cre) on an *Apoe*<sup>KO</sup> background (Supporting Information Table S5). The specificity of the knockdown in MAECs was detected in Supporting Information Fig. S4A and S4B. To evaluate the potential influence of sex on our study results, we performed additional analyses. To determine sex-based differences, male and female mice were examined separately. By staining with Oil Red O, we compared the extent of atherosclerosis in the entire aorta using Image-Pro Plus software, and we found that the sex of the mice did not significantly affect the observed outcomes. In the atherosclerosis model, irrespective of sex, *Apoe*<sup>KO</sup>*Asf1a*<sup>ECKO</sup> mice showed reduced progression of

stained with CD31 (green) and  $\alpha$ -SMA (red); nuclei counterstained with DAPI (blue) ( $n = 6$  mice per group). Scale bar, 50  $\mu$ m. (E) Western blot analysis of Pan K1a and H3K181a in the MAECs extracted from HFD-fed *Apoe*<sup>KO</sup> after 2-DG treatment ( $n = 6$  mice per group). (F) RT-qPCR analysis of EndMT markers in MAECs extracted from HFD-fed *Apoe*<sup>KO</sup> after 2-DG treatment ( $n = 10$  mice per group). (G) ChIP analysis of the enrichment of P300 and H3K181a at the promoter region of *Snai1* in MAECs extracted from HFD-fed *Apoe*<sup>KO</sup> after 2-DG treatment ( $n = 6$  mice per group). (H) Re-ChIP was performed with the first round with H3K181a antibody and a second round of pull-down with P300 antibodies in MAECs extracted from HFD-fed *Apoe*<sup>KO</sup> after 2-DG treatment ( $n = 6$  mice per group). (A)–(C), (G), and (H) were analyzed by unpaired two-tailed student's *t*-test. (E) and (F) were analyzed by unpaired *t*-test with Welch's correction. Data are shown as mean  $\pm$  SD; \*\**P* < 0.01, \*\*\**P* < 0.001; ns, not significant. HDL-C: high-density lipoprotein cholesterol; LDL-C: low-density lipoprotein cholesterol; T-CHO: total cholesterol; TG: triglyceride.

atherosclerosis lesions in the aortas when compared with controls (Fig. 5C and Fig. S4C). Therefore, in subsequent experiments with a reduced sample size, we focused solely on male mice. We found that *Apoe*<sup>KO</sup>*Asf1a*<sup>ECKO</sup> mice had a considerably less necrotic core, reduced lipid burden in total artery and root sections, and increased collagen content relative to *Apoe*<sup>KO</sup>*Asf1a*<sup>WT</sup> mice (Fig. 5C, D, and Fig. S4C). Besides, the EC marker CD31 was significantly downregulated in the vessels of HFD-fed *Apoe*<sup>KO</sup>*Asf1a*<sup>WT</sup> mice, while  $\alpha$ -SMA had the contrary phenomenon (Fig. 5E). Enface staining showed significantly reduced levels of H3K18la expression in *Apoe*<sup>KO</sup>*Asf1a*<sup>ECKO</sup> mice relative to *Apoe*<sup>KO</sup>*Asf1a*<sup>WT</sup> mice (Fig. 5F).

To determine the effect of endothelial cell-specific *Asf1a* knockdown at the cellular level, we cultured MAECs from NC-fed or HFD-fed *Apoe*<sup>KO</sup>*Asf1a*<sup>WT</sup> and *Apoe*<sup>KO</sup>*Asf1a*<sup>ECKO</sup> mice. We found that the cell morphology of ECs derived from *Apoe*<sup>KO</sup>*Asf1a*<sup>ECKO</sup> mice was significantly altered compared to *Apoe*<sup>KO</sup>*Asf1a*<sup>WT</sup> mice (Fig. 5G). The acidification rate of ECs from *Apoe*<sup>KO</sup>*Asf1a*<sup>ECKO</sup> mice did not change significantly compared with *Apoe*<sup>KO</sup>*Asf1a*<sup>WT</sup> mice, demonstrating that ASF1A mainly regulates the modification of H3K18la and has no major effect on lactate content (Fig. 5H). Meanwhile, ECs-specific knockout of *Asf1a* could significantly inhibit the EndMT process, which further confirmed the crucial role of endothelial ASF1A in histone lactylation and the EndMT phenotype (Fig. 5I, J, and Fig. S4D). Consistently, the enrichment of H3K18la or P300 at the *Snail* promoter was significantly reduced in ECs from *Apoe*<sup>KO</sup>*Asf1a*<sup>ECKO</sup> mice (Fig. 5K). Besides, the interaction between the *Snail* promoter and H3K18la was significantly affected by *Asf1a* deficiency (Fig. 5L). Re-ChIP analysis further confirmed that the enrichment of H3K18la and P300 at the *Snail* promoter was suppressed by the *Asf1a* deficiency (Fig. 5M). In conclusion, these findings suggest that ASF1A facilitates the binding of P300 and H3K18la to the *Snail* promoter region, which facilitates the mouse endothelium cells' transition to the EndMT phenotype.

### 3.6. Pharmacological inhibition of lactate levels reduces EndMT and atherosclerosis in *Apoe*<sup>KO</sup> mice

To investigate whether inhibiting glycolysis will impact atherosclerosis disease progression, we employed a competitive inhibitor of hexokinase 2-deoxy-glucose to examine the effect of glycolysis inhibition in a model of atherosclerosis using HFD-fed *Apoe*<sup>KO</sup> mice. We compared 2-DG-fed *Apoe*<sup>KO</sup> mice with conventional *Apoe*<sup>KO</sup> mice and found no change in their lipid levels, as well as blood glucose and blood routine levels (Fig. 6A, Supporting Information Fig. S5A and Table S6). Mice fed 2-DG showed much less lipid-filled damage (Fig. 6B). Oil Red O, H&E, Masson, and Sirius Red staining of mouse aortic roots showed that 2-DG significantly inhibited atherosclerosis caused by histone lactylation (Fig. 6C). As shown in Fig. 6D, compared with HFD group, double immunofluorescence staining showed a significant reduction in co-localization of CD31 and  $\alpha$ -SMA and a significant increase in CD31 continuity after 2-DG treatment. These results indicated that 2-DG blocked the development of HFD-induced EndMT, and improved the impairment of the aortic endothelial barrier (Fig. 6D). We also extracted ECs for cultivation and found a reduced level of H3K18la, increased expression of endothelial cell markers, and decreased expression of mesenchymal cell markers in 2-DG-fed mice (Fig. 6E and F). The enrichment of H3K18la and P300 at the *Snail* promoter was also verified by ChIP and Re-ChIP analyses, which revealed

significantly reduced expression levels of H3K18la and P300 in 2-DG-fed mice (Fig. 6G and H). The above results suggest that histone lactylation enhances *Snail* transcriptional activity, leading to the development and progression of atherosclerosis.

### 3.7. PROTAC HK2 Degradator-1 reduces EndMT and atherosclerosis in *Apoe*<sup>KO</sup> mice

2-DG, a traditional inhibitor of Hexokinase, is a glucose analog that inhibits glycolysis by acting on hexokinase. Hexokinase 2 (HK2) is the major rate-limiting enzyme in the aerobic glycolytic pathway and plays an important role in promoting the Warburg effect. Studies have found limited efficacy with 2-DG because endogenous glucose competes with it for the active site of hexokinase<sup>42</sup>. In recent years, PROTAC has emerged as a promising technique for targeted protein degradation. Therefore, we employed a newly developed HK2 degrader (PROTAC HK2 Degradator-1) synthesized by PROTAC technology to precisely degrade HK2 and inhibit the increase in lactate caused by aerobic glycolysis (Fig. 7A)<sup>42</sup>. As shown in Fig. 7B, PROTAC HK2 Degradator-1 induced HK2 degradation in HCAECs in a dose-dependent manner, and the hook effect occurred at concentrations up to 50  $\mu$ mol/L. PROTAC HK2 Degradator-1 could promote HK2 protein degradation within 12 h, with the greatest degradation effect at 36 h (Fig. 7C). The results of the cell counting kit-8 (CCK-8) assay showed PROTAC HK2 Degradator-1 had little effect on the growth of HCAECs (Fig. 7D). Treatment with MG132, a powerful proteasome inhibitor, prevented PROTAC HK2 Degradator-1-induced HK2 degradation, confirming that PROTAC HK2 Degradator-1 degrades HK2 protein through the ubiquitin-proteasome system by forming a ternary complex (Fig. 7E). HK1 is used for glucose utilization in normal tissues and therefore should not be inhibited. We therefore examined the effect of PROTAC HK2 Degradator-1 on HK1 degradation to assess its selectivity for HK2. As shown in Fig. 7F, PROTAC HK2 Degradator-1 selectively disrupted HK2 with no effect on the amount of HK1 protein in the cell. PROTAC HK2 Degradator-1 significantly reduced the increase in lactate in ox-LDL-stimulated HCAEC (Fig. 7G), confirming that PROTAC HK2 Degradator-1 degrades HK2 protein and inhibits aerobic glycolysis in ECs. In conclusion, PROTAC HK2 Degradator-1 can block the aerobic glycolytic process of HCAECs and reduce lactate production by precisely degrading HK2 protein. We further performed an *in vivo* study to examine the efficacy of PROTAC HK2 Degradator-1 on the atherosclerosis model established in high-fat-fed *Apoe*<sup>KO</sup> mice. As shown in Fig. 7H, PROTAC HK2 Degradator-1 reduced aortic lipid damage in high-fat-fed *Apoe*<sup>KO</sup> mice compared with vehicle. Oil red O, H&E, Masson, and Sirius Red staining of mouse aortic roots showed that PROTAC HK2 Degradator-1 significantly reduced the severity of atherosclerosis in mice (Fig. 7I and J). Extraction of MAECs revealed reduced levels of H3K18la, increased expression of endothelial cell markers, and decreased expression of mesenchymal cell markers in mice injected with PROTAC HK2 Degradator-1, which further verified the efficacy of PROTAC HK2 Degradator-1 (Fig. 7K and L). In addition, the lipid levels, blood glucose levels, and blood routine levels of the PROTAC-injected *Apoe*<sup>KO</sup> mice did not change compared with the uninjected ones, and there was no obvious decrease in body weight, indicating that the mice tolerated PROTAC HK2 Degradator-1 well (Supporting Information Fig. S5B and Table S7). These results demonstrate the efficacy of PROTAC HK2 Degradator-1 in inhibiting the development of atherosclerosis,

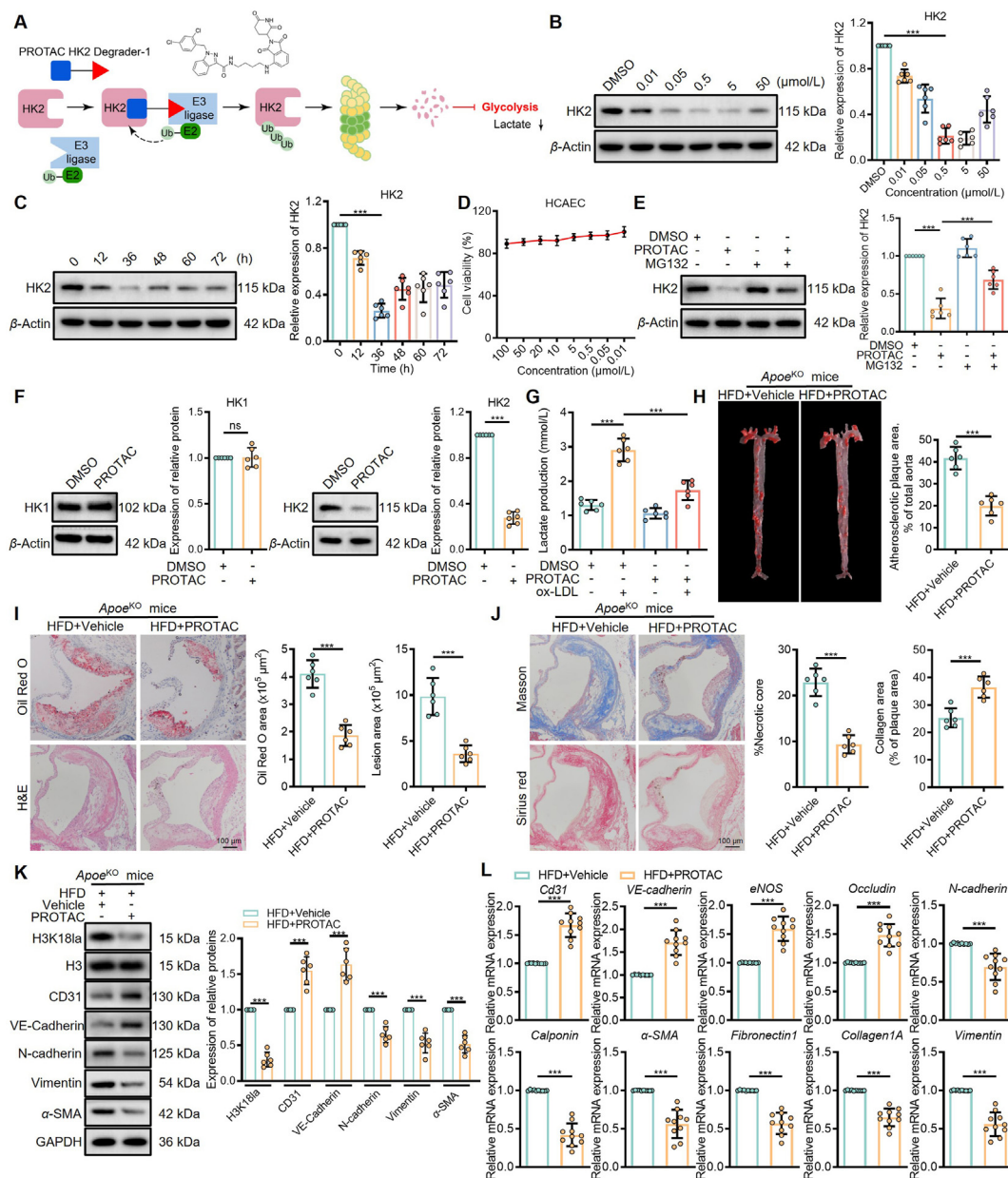


**Figure 7** PROTAC HK2 Degrader-1 reduces EndMT and atherosclerosis in *Apoe*<sup>KO</sup> mice. (A) Chemical Structure and schematic of PROTAC HK2 Degrader-1 mode of action. (B) Western blot analysis of HK2 in HCAECs treated with the indicated concentration of PROTAC HK2 Degrader-1 for 36 h ( $n = 6$ ). (C) Western blot analysis of HK2 in HCAECs treated with 0.5  $\mu\text{mol/L}$  PROTAC HK2 Degrader-1 for the indicated incubation time ( $n = 6$ ). (D) Viability of HCAECs after treatment with PROTAC HK2 Degrader-1 for 48 h by CCK-8 assay ( $n = 6$ ). (E) Western blot analysis of HK2 in HCAECs pretreated with 2  $\mu\text{mol/L}$  MG132 for 2 h before being treated with 0.5  $\mu\text{mol/L}$  PROTAC HK2 Degrader-1 for 36 h ( $n = 6$ ). (F) Western blot analysis of HK1 and HK2 protein levels in HCAECs after incubation with 0.5  $\mu\text{mol/L}$  PROTAC HK2 Degrader-1 for 36 h. ( $n = 6$ ). (G) Lactate level of HCAECs treated with 0.5  $\mu\text{mol/L}$  PROTAC HK2 Degrader-1 for 36 h ( $n = 6$ ). (H) Representative images of aortas stained with Oil Red O from HFD-fed *Apoe*<sup>KO</sup> mice given intraperitoneal injections with Vehicle control or PROTAC HK2 Degrader-1 (5 mg/kg, q.o.d. for 12 weeks). The quantitative data of Oil Red O staining of mouse blood vessels ( $n = 6$  mice per group). (I, J) Atherosclerotic lesion formation detected by H&E, Oil Red O, Sirius red, and Masson's trichrome staining ( $n = 6$  mice per group). Scale bar, 100  $\mu\text{m}$ . Quantification of lesions area and Oil Red O area. Percentage of necrotic core and collagen area. (K) Western blot analysis of H3K181a and EndMT markers in the MAECs extracted from HFD-fed *Apoe*<sup>KO</sup> after PROTAC HK2 Degrader-1 treatment ( $n = 6$  mice per group). (L) RT-qPCR analysis of EndMT markers in MAECs extracted from HFD-fed *Apoe*<sup>KO</sup> after PROTAC HK2 Degrader-1 treatment ( $n = 10$  mice per group). (B), (C), (D), (E), and (G) were analyzed by Ordinary one-way ANOVA with Tukey's multiple comparisons test. (H)–(J) were analyzed by unpaired two-tailed student's *t*-test. (K), (F), and (L) were analyzed by unpaired *t*-test with Welch's correction. Data are shown as mean  $\pm$  SD; \*\* $P < 0.01$ , \*\*\* $P < 0.001$ ; ns, not significant. PROTAC: proteolysis-targeting chimera; HK2: Hexokinase 2.

which could contribute to the development of promising therapeutic strategies for atherosclerosis and CVDs.

### 3.8. H3K18la and ASF1A may be clinically involved in EndMT and atherosclerosis

Finally, we examined protein lactylation levels in patients with atherosclerosis and their possible clinical significance. Patients with atherosclerosis had significantly higher plasma lactate levels

(Fig. 8A). Western blot results showed higher levels of Pan K1a and H3K18la in aortic tissues from atherosclerotic patients than in control subjects (non-atherosclerotic patients), accompanied by decreased levels of endothelial markers. Notably, P300, SNAI1, and ASF1A levels were also significantly elevated in atherosclerotic patients (Fig. 8B). Consistent with the Western blot results, the mRNA levels of endothelial markers, such as *CD31* and VE-cadherin, were markedly decreased compared with the control, while *SNAI1* and *ASF1A* expression were increased in

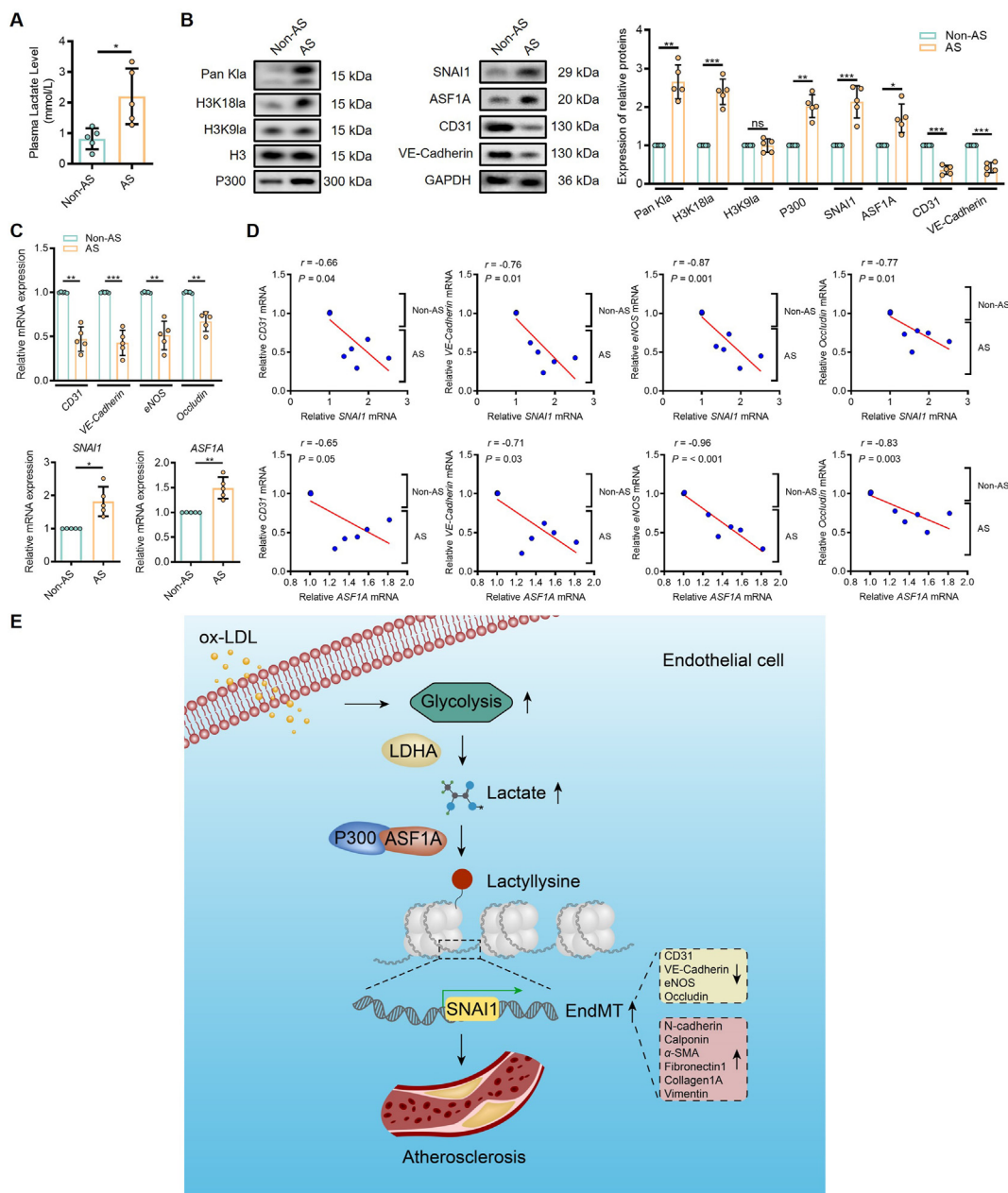


**Figure 8** H3K18la and ASF1A may be clinically involved in EndMT and atherosclerosis. (A) Plasma lactate level in patients with atherosclerosis ( $n = 5$  human samples per group). (B) Pan K1a, H3K18la, H3K9la, P300, endothelial-like cell markers VE-cadherin and CD31, SNAI1, and ASF1A levels were detected in human atherosclerotic arteries by Western blot ( $n = 5$  human samples per group). (C) RT-qPCR analysis of vascular endothelial markers, *ASF1A*, and *SNAI1* in human atherosclerotic arteries ( $n = 5$  human samples per group). (D) Linear regression analysis of *SNAI1* and *ASF1A* with EndMT markers. (E) Model of the crosstalk between glycolysis metabolism and H3K18la, detailed in discussion. (A) was analyzed by unpaired two-tailed student's *t*-test. (B) and (C) were analyzed by unpaired *t*-test with Welch's correction. Data are shown as mean  $\pm$  SD; \* $P < 0.05$ , \*\* $P < 0.01$ , \*\*\* $P < 0.001$ ; ns, not significant.

human atherosclerotic arteries (Fig. 8C). Linear regression analysis revealed that changes in mRNA levels of endothelial markers were closely associated with *SNAI1* and *ASF1A* (Fig. 8D). Collectively, the results suggest that H3K18la and ASF1A may be clinically involved in EndMT and atherosclerosis.

#### 4. Discussion

There is mounting evidence that EndMT has an essential role in cardiovascular disorders<sup>7</sup>. Our studies suggest that histone lactylation plays an important role in the regulation of EndMT. Ox-LDL induces an abnormal elevation of aerobic glycolysis in vascular ECs, causing lactate accumulation. ASF1A and P300 together regulate histone H3K18 lactylation, which increases the expression of *SNAI1*, a transcription factor of EndMT, inducing EndMT and promoting atherosclerosis. Our study elucidates a previously unidentified epigenetic mechanism that ox-LDL stimulates, leading to increased aerobic glycolysis of ECs and increased lactate, contributing to an increment in histone lactylation. Histone acetylase P300 forms a chromatin microenvironment characterized by enrichment of H3K18la with the help of histone chaperone ASF1A, which triggers EndMT by increasing the expression of *SNAI1*, ultimately leading to atherogenesis. These findings suggest that ASF1A may also be a potentially valuable drug target for CVDs (Fig. 8).

The Warburg effect is one of the most extensively researched types of cellular metabolic reprogramming. It makes tumor cells use glycolysis to produce energy to maintain their aggressiveness and proliferation, rather than oxidative phosphorylation<sup>43</sup>. Metabolic reprogramming involves various metabolic pathways, such as gluconeogenesis, lipid metabolism, and amino acid metabolism, that are closely linked to the development of disease. Recently, it has been found that the Warburg effect plays an essential role in endothelial dysfunction and atherosclerosis, as the endothelium is predominantly glycolytic as an energy source<sup>44</sup>. It has been reported that there is increased glycolysis production at arterial branches and vessel wall irregularities because of oscillatory shear stress, which results in endothelial dysfunction and atherosclerosis<sup>45</sup>. The above studies suggested that the atherosclerotic endothelium is prone to the Warburg effect, leading to lactate accumulation and inducing EndMT. Based on these previous studies, we hypothesize that lactate is involved in EndMT-induced atherosclerosis. Here, we found an increased level of lactate in ox-LDL-treated ECs. The ECs treated with ox-LDL underwent a morphological change from a cobblestone-like endothelial phenotype to a spindle-shaped mesenchymal phenotype, as identified by cytomorphology, which was reversed after administration of glycolysis inhibitors and lactate dehydrogenase inhibitor treatment. Therefore, we confirm that ox-LDL promotes EndMT by elevating lactate, leading to atherosclerosis.

Post-translational modification plays a vital role in chromatin function and epigenetic regulation, including phosphorylation, methylation, and acetylation, which are closely related to a variety of diseases<sup>46</sup>. Recently, a novel histone modification called histone lactylation was found to be regulated by lactate content in cells and has been shown to directly stimulate gene transcription<sup>24</sup>. However, the role of histone lactylation in atherosclerosis is unclear. Up to now, 28 lactylation sites on the core histone have been found, including H3K9, H3K18, H4K12, etc.<sup>24</sup>. This diversity of histone lactylation is highly correlated with the occurrence of

specific diseases. H3K9la and H3K56la were found to promote tumorigenesis<sup>47</sup>, and H3K18la contributes to tumorigenesis by facilitating YTHDF2 expression<sup>25</sup>. In addition, H4K12la, glycolysis, and PKM2 formation positive feedback circuits aggravate microglia dysfunction<sup>26</sup>. However, screening in our study revealed the most significant differences in H3K18la. Eventually, we confirmed that histone lactylation, mainly H3K18la, is involved in EndMT atherosclerosis. Supported by similar studies, H3K18la can increase *Mettl3* expression to improve the immunosuppressive ability of tumor-infiltrating myeloid cells<sup>48</sup>. It has also been reported that H3K18 is an essential disease-modifying site for septic shock<sup>49</sup>. These studies suggested that H3K18la is a characteristic histone marker and is specifically associated with disease.

The alteration of the tissue microenvironment, an important determinant of cell behavior and physiological function, can lead to many diseases. It is well known that histone lactylation of macrophages is essential for anti-inflammation and restoration of homeostasis and has been studied in diseases such as cardiac hypertrophy<sup>50</sup> and intestinal inflammation<sup>51</sup>. However, histone lactylation is also involved in the early regulation of disease development, such as Alzheimer's disease<sup>26</sup> and pulmonary hypertension<sup>27</sup>. In our study, histone lactylation was considered a risk factor for promoting atherosclerosis. We suggest that histone lactylation plays a distinct role in the tissue and its surrounding microenvironment. The tissue microenvironment influences changes in metabolites such as lactate, which is produced during energy reprogramming and causes changes in the chromatin microenvironment by histone lactylation modifications that switch and promote transcriptional expression of genes at the chromatin level<sup>32</sup>.

We present a chromatin microenvironment composed of H3K18la, which can specifically label and mediate the degree of gene expression of *SNAI1*. HAT P300, histone acetyltransferase, is a potential histone lysine lactylation "writer" protein. We identified catalytic activities from three major HDAC families and P300 in the regulation of histone lactylation in ECs and clarified the important relevance of P300, which has been shown in myocardial infarction and sepsis as well<sup>50</sup>. Until today, whether P300-dependent histone lactylation requires a cofactor to precisely regulate specific target genes remained a mystery. ASF1A is a histone chaperone that participates in chromatin higher-order organization. There is evidence that P300 and ASF1A can coexist in *Drosophila* and HeLa cells<sup>53</sup>, and by correlation experimental analysis, we found that it is indeed a cofactor of P300 and that H3K18la depends on it in ECs. Previous studies have shown that ASF1A plays a key role in tumor development and progression<sup>54</sup>, and accelerates chronic myeloid leukemia by activating Notch signaling<sup>55</sup>, but has not been reported in the cardiovascular field. Here, our study provided the first evidence that P300 and ASF1A can form a characteristic complex to precisely regulate the expression of *SNAI1* by specifically activating the lactylation of histone H3 lysine 18, broadening the understanding of histone chaperones as drug target proteins for atherosclerosis.

Our present findings confirm that 2-DG can restore EndMT occurring in vascular endothelial cells damaged by ox-LDL by regulating ASF1A-dependent P300-mediated H3K18 lactylation, thereby ameliorating atherosclerosis. 2-DG has also undergone extensive testing in clinical trials against various cancers and has been explored or tested as an adjuvant to various clinical chemotherapeutic agents for a variety of cancer types such as

glioma, breast cancer, lung cancer, etc.<sup>56</sup>. 2-DG has been approved as an adjunctive treatment for patients with moderate to severe COVID-19. COVID-19 patients who received 2-DG treatment showed significant improvement in their symptoms<sup>57</sup>. Our results demonstrated that 2-DG reduces histone lactylation by inhibiting glycolysis to reduce lactate production, which in turn decreases the occupancy of H3K18la at the promoter of *SNAIL1*, the transcription factor of EndMT, through various epigenetic mechanisms, leading to downregulation of EndMT. These findings implicate 2-DG as a potential therapeutic agent for atherosclerosis.

In view of the fact that endogenous glucose competes with 2-DG for the active site of hexokinase, a cutting-edge targeted protein proteolysis technology, the PROTAC, was used in our experiments to inhibit atherosclerosis through the potent degradation of Hexokinase, which was superior to inhibitors. PROTAC, consisting of two covalently linked molecules, binds both the target protein and the E3 ligase, thereby inducing protein proteolysis of the target protein *via* the ubiquitin–proteasome system. Here, we found that the PROTAC HK2 Degradator-1 effectively degraded Hexokinase, and inhibited lactate production, which in turn significantly reduced endothelial histone H3K18 lactylation, and inhibited EndMT of ECs in response to disease stimuli. In addition, PROTAC HK2 Degradator-1 was bioavailable and contributed to attenuating the development of atherosclerosis in mice. These findings suggest that the degradation of Hexokinase by PROTAC can effectively inhibit the aerobic metabolism of ECs, thereby inhibiting their EndMT and endothelial dysfunction and thus alleviating the progression of atherosclerosis.

The present study has several limitations. Unlike humans, mouse models for atherosclerosis rarely exhibit plaque rupture and thrombus occlusion, and thus we only indirectly assessed the effect of ASF1A on plaque progression and instability using metrics such as lipid content in plaques and percentage of necrotic core area. In addition, the physiology of human arteries cannot be replicated exactly with human cells or mouse arteries, and further work is needed to improve the translational applicability of our findings, which should test new models that are closer to the human condition.

Our study reveals a previously unidentified mechanism of epigenetic regulation of atherosclerosis by EndMT that couples the reprogramming of energy metabolism and epigenetics, in which histone lactylation driven by glycolytic metabolism plays a central role. The epigenetic microenvironment plays an emerging role in the changes of EndMT and atherosclerosis progression, which provides us with unprecedented drug targets for future studies of disease mechanisms.

## 5. Conclusions

We identified for the first time that P300 and ASF1A activate the transcription factor of EndMT through H3K18la modification, which in turn leads to endothelial dysfunction, linking histone lactylation to EndMT and atherosclerosis. This is an innovative model through which a promising strategy for atherosclerosis treatment and drug regimens is provided, casting a new light on the treatment of atherosclerosis-related CVDs.

## Acknowledgments

This study was supported by the National Natural Science Foundation of China (82270421, 81970428, 31771334, 81800385,

82270484, 82370376, 82121001, 82030013, and 82241211), Major Research Plan of the National Natural Science Foundation of China (91649125), the National Key R&D Program of China (2019YFA0802704), The major project of Natural Science Foundation of the Jiangsu Higher Education Institution of China (21KJA310006), Jiangsu Provincial Social Development Project (BE2021749, China), Special Program for Top Innovative Talents (NJMUTY20230082, China).

## Author contributions

Mengdie Dong: Conceptualization, Writing-original draft. Yunjia Zhang: Formal analysis, Writing-original draft. Minghong Chen: Formal analysis, Writing-original draft. Yongkang Tan: Validation. Jiao Min: Validation. Xian He: Validation. Fuhao Liu: Validation. Jiaming Gu: Methodology. Hong Jiang: Visualization. Longbin Zheng: Investigation. Jiaping Chen: Methodology. Quanwen Yin: Data curation. Xuesong Li: Project administration. Xiang Chen: Investigation. Yongfeng Shao: Conceptualization. Yong Ji: Conceptualization. Hongshan Chen: Conceptualization, Writing-review & editing.

## Conflicts of interest

The authors declare no conflicts of interest.

## Appendix A. Supporting information

Supporting information to this article can be found online at <https://doi.org/10.1016/j.apsb.2024.03.008>.

## References

- Herrington W, Lacey B, Sherliker P, Armitage J, Lewington S. Epidemiology of atherosclerosis and the potential to reduce the global burden of atherothrombotic disease. *Circ Res* 2016;**118**:535–46.
- Cen X, Wang B, Liang Y, Chen Y, Xiao Y, Du S, et al. Small molecule SMU-CX24 targeting toll-like receptor 3 counteracts inflammation: a novel approach to atherosclerosis therapy. *Acta Pharm Sin B* 2022;**12**:3667–81.
- Xu S, Ilyas I, Little PJ, Li H, Kamato D, Zheng X, et al. Endothelial dysfunction in atherosclerotic cardiovascular diseases and beyond: from mechanism to pharmacotherapies. *Pharmacol Rev* 2021;**73**:924–67.
- Li X, Chen X, Zheng L, Chen M, Zhang Y, Zhu R, et al. Non-canonical STING–PERK pathway dependent epigenetic regulation of vascular endothelial dysfunction *via* integrating IRF3 and NF- $\kappa$ B in inflammatory response. *Acta Pharm Sin B* 2023;**13**:4765–84.
- Bischoff J. Endothelial-to-mesenchymal transition. *Circ Res* 2019;**124**:1163–5.
- Piera-Velazquez S, Jimenez SA. Endothelial to mesenchymal transition: role in physiology and in the pathogenesis of human diseases. *Physiol Rev* 2019;**99**:1281–324.
- Kovacic JC, Dimmeler S, Harvey RP, Finkel T, Aikawa E, Krenning G, et al. Endothelial to mesenchymal transition in cardiovascular disease: JACC state-of-the-art review. *J Am Coll Cardiol* 2019;**73**:190–209.
- Souilhol C, Harmsen MC, Evans PC, Krenning G. Endothelial–mesenchymal transition in atherosclerosis. *Cardiovasc Res* 2018;**114**:565–77.
- Lecce L, Xu Y, V'Gangula B, Chandel N, Pothula V, Caudrillier A, et al. Histone deacetylase 9 promotes endothelial–mesenchymal transition and an unfavorable atherosclerotic plaque phenotype. *J Clin Invest* 2021;**131**:e131178.

10. Thakur C, Chen F. Connections between metabolism and epigenetics in cancers. *Semin Cancer Biol* 2019;**57**:52–8.
11. Archer SL. Pyruvate kinase and warburg metabolism in pulmonary arterial hypertension: uncoupled glycolysis and the cancer-like phenotype of pulmonary arterial hypertension. *Circulation* 2017;**136**:2486–90.
12. Gao C, Wang Y. YAP: the nexus between metabolism and cardiac remodeling. *J Clin Invest* 2022;**132**:e157664.
13. González-Rodríguez P, Zampese E, Stout KA, Guzman JN, Ilijic E, Yang B, et al. Disruption of mitochondrial complex I induces progressive parkinsonism. *Nature* 2021;**599**:650–6.
14. Hsu PP, Sabatini DM. Cancer cell metabolism: warburg and beyond. *Cell* 2008;**134**:703–7.
15. Feng S, Bowden N, Fragiadaki M, Souilhol C, Hsiao S, Mahmoud M, et al. Mechanical activation of hypoxia-inducible factor 1 $\alpha$  drives endothelial dysfunction at atheroprone sites. *Arterioscler Thromb Vasc Biol* 2017;**37**:2087–101.
16. Fan M, Yang K, Wang X, Chen L, Gill PS, Ha T, et al. Lactate promotes endothelial-to-mesenchymal transition via Snail1 lactylation after myocardial infarction. *Sci Adv* 2023;**9**:eadc9465.
17. Napoli C, Benincasa G, Loscalzo J. Epigenetic inheritance underlying pulmonary arterial hypertension. *Arterioscler Thromb Vasc Biol* 2019;**39**:653–64.
18. Shi Y, Zhang H, Huang S, Yin L, Wang F, Luo P, et al. Epigenetic regulation in cardiovascular disease: mechanisms and advances in clinical trials. *Signal Transduct Target Ther* 2022;**7**:200.
19. Lin Z, Zhao S, Li X, Miao Z, Cao J, Chen Y, et al. Cathepsin B S-nitrosylation promotes ADAR1-mediated editing of its own mRNA transcript via an ADD1/MATR3 regulatory axis. *Cell Res* 2023;**33**:546–61.
20. Kouzarides T. Chromatin modifications and their function. *Cell* 2007;**128**:693–705.
21. Lawrence M, Daujat S, Schneider R. Lateral thinking: how histone modifications regulate gene expression. *Trends Genet* 2016;**32**:42–56.
22. Gao P, You M, Li L, Zhang Q, Fang X, Wei X, et al. Salt-induced hepatic inflammatory memory contributes to cardiovascular damage through epigenetic modulation of SIRT3. *Circulation* 2022;**145**:375–91.
23. Duan S, Lou X, Chen S, Jiang H, Chen D, Yin R, et al. Macrophage LMO7 deficiency facilitates inflammatory injury via metabolic-epigenetic reprogramming. *Acta Pharm Sin B* 2023;**13**:4785–800.
24. Zhang D, Tang Z, Huang H, Zhou G, Cui C, Weng Y, et al. Metabolic regulation of gene expression by histone lactylation. *Nature* 2019;**574**:575–80.
25. Yu J, Chai P, Xie M, Ge S, Ruan J, Fan X, et al. Histone lactylation drives oncogenesis by facilitating m<sup>6</sup>A reader protein YTHDF2 expression in ocular melanoma. *Genome Biol* 2021;**22**:85.
26. Pan RY, He L, Zhang J, Liu X, Liao Y, Gao J, et al. Positive feedback regulation of microglial glucose metabolism by histone H4 lysine 12 lactylation in Alzheimer's disease. *Cell Metab* 2022;**34**:634–48.e6.
27. Chen J, Zhang M, Liu Y, Zhao S, Wang Y, Wang M, et al. Histone lactylation driven by mROS-mediated glycolytic shift promotes hypoxic pulmonary hypertension. *J Mol Cell Biol* 2023;**13**:mjac073.
28. Eelen G, de Zeeuw P, Treps L, Harjes U, Wong BW, Carmeliet P. Endothelial cell metabolism. *Physiol Rev* 2018;**98**:3–58.
29. Rask-Madsen C, Li Q, Freund B, Feather D, Abramov R, Wu IH, et al. Loss of insulin signaling in vascular endothelial cells accelerates atherosclerosis in apolipoprotein E null mice. *Cell Metab* 2010;**11**:379–89.
30. Roberts TC, Hart JR, Kaikkonen MU, Weinberg MS, Vogt PK, Morris KV. Quantification of nascent transcription by bromouridine immunocapture nuclear run-on RT-qPCR. *Nat Protoc* 2015;**10**:1198–211.
31. Hagège H, Klous P, Braem C, Splinter E, Dekker J, Cathala G, et al. Quantitative analysis of chromosome conformation capture assays (3C-qPCR). *Nat Protoc* 2007;**2**:1722–33.
32. Tzoulaki I, Castagné R, Boulangé CL, Karaman I, Chekmeneva E, Evangelou E, et al. Serum metabolic signatures of coronary and carotid atherosclerosis and subsequent cardiovascular disease. *Eur Heart J* 2019;**40**:2883–96.
33. Sun JX, Chang TF, Li MH, Sun LJ, Yan XC, Yang ZY, et al. SNAI1, an endothelial–mesenchymal transition transcription factor, promotes the early phase of ocular neovascularization. *Angiogenesis* 2018;**21**:635–52.
34. Li X, Zhang Z, Zhang Y, Cao Y, Wei H, Wu Z. Upregulation of lactate-inducible snail protein suppresses oncogene-mediated senescence through p16<sup>INK4a</sup> inactivation. *J Exp Clin Cancer Res* 2018;**37**:39.
35. Moreno-Yruela C, Zhang D, Wei W, Bæk M, Liu W, Gao J, et al. Class I histone deacetylases (HDAC1–3) are histone lysine deacetylases. *Sci Adv* 2022;**8**:eabi6696.
36. Zhang Q, Vo N, Goodman RH. Histone binding protein RbAp48 interacts with a complex of CREB binding protein and phosphorylated CREB. *Mol Cell Biol* 2000;**20**:4970–8.
37. Kaypee S, Sahadevan SA, Sudarshan D, Halder Sinha S, Patil S, Senapati P, et al. Oligomers of human histone chaperone NPM1 alter p300/KAT3B folding to induce autoacetylation. *Biochim Biophys Acta Gen Subj* 2018;**1862**:1729–41.
38. Shimada M, Chen WY, Nakadai T, Onikubo T, Guermah M, Rhodes D, et al. Gene-specific H1 eviction through a transcriptional activator p300/NAP1H1 pathway. *Mol Cell* 2019;**74**:268–83.e5.
39. Das C, Roy S, Namjoshi S, Malarkey CS, Jones DN, Kutateladze TG, et al. Binding of the histone chaperone ASF1 to the CBP bromodomain promotes histone acetylation. *Proc Natl Acad Sci U S A* 2014;**111**:E1072–81.
40. Gonzalez-Muñoz E, Arboleda-Estudillo Y, Otu HH, Cibelli JB. Cell reprogramming. Histone chaperone ASF1A is required for maintenance of pluripotency and cellular reprogramming. *Science* 2014;**345**:822–5.
41. Mousson F, Lautrette A, Thuret JY, Agez M, Courbeyrette R, Amigues B, et al. Structural basis for the interaction of Asf1 with histone H3 and its functional implications. *Proc Natl Acad Sci U S A* 2005;**102**:5975–80.
42. Sang R, Fan R, Deng A, Gou J, Lin R, Zhao T, et al. Degradation of hexokinase 2 blocks glycolysis and induces GSDME-dependent pyroptosis to amplify immunogenic cell death for breast cancer therapy. *J Med Chem* 2023;**66**:8464–83.
43. Koppenol WH, Bounds PL, Dang CV. Otto Warburg's contributions to current concepts of cancer metabolism. *Nat Rev Cancer* 2011;**11**:325–37.
44. Rohlenova K, Veys K, Miranda-Santos I, De Bock K, Carmeliet P. Endothelial cell metabolism in health and disease. *Trends Cell Biol* 2018;**28**:224–36.
45. Han Y, He M, Marin T, Shen H, Wang WT, Lee TY, et al. Roles of KLF4 and AMPK in the inhibition of glycolysis by pulsatile shear stress in endothelial cells. *Proc Natl Acad Sci U S A* 2021;**118**:e2103982118.
46. Gupta R, Sahu M, Srivastava D, Tiwari S, Ambasta RK, Kumar P. Post-translational modifications: regulators of neurodegenerative proteinopathies. *Ageing Res Rev* 2021;**68**:101336.
47. Pan L, Feng F, Wu J, Fan S, Han J, Wang S, et al. Demethylzylalsteral targets lactate by inhibiting histone lactylation to suppress the tumorigenicity of liver cancer stem cells. *Pharmacol Res* 2022;**181**:106270.
48. Xiong J, He J, Zhu J, Pan J, Liao W, Ye H, et al. Lactylation-driven METTL3-mediated RNA m<sup>6</sup>A modification promotes immunosuppression of tumor-infiltrating myeloid cells. *Mol Cell* 2022;**82**:1677–77.e10.
49. Chu X, Di C, Chang P, Li L, Feng Z, Xiao S, et al. Lactylated histone H3K18 as a potential biomarker for the diagnosis and predicting the severity of septic shock. *Front Immunol* 2021;**12**:786666.
50. Wang N, Wang W, Wang X, Mang G, Chen J, Yan X, et al. Histone lactylation boosts reparative gene activation post-myocardial infarction. *Circ Res* 2022;**131**:893–908.
51. Irizarry-Caro RA, McDaniel MM, Overcast GR, Jain VG, Troutman TD, Pasare C. TLR signaling adapter BCAP regulates inflammatory to reparatory macrophage transition by promoting histone lactylation. *Proc Natl Acad Sci U S A* 2020;**117**:30628–38.
52. Li L, Chen K, Wang T, Wu Y, Xing G, Chen M, et al. Glis1 facilitates induction of pluripotency via an epigenome–metabolome–epigenome signalling cascade. *Nat Metab* 2020;**2**:882–92.

53. Das C, Lucia MS, Hansen KC, Tyler JK. CBP/p300-mediated acetylation of histone H3 on lysine 56. *Nature* 2009;**459**:113–7.
54. Liang X, Yuan X, Yu J, Wu Y, Li K, Sun C, et al. Histone chaperone ASF1A predicts poor outcomes for patients with gastrointestinal cancer and drives cancer progression by stimulating transcription of  $\beta$ -catenin target genes. *EBioMedicine* 2017;**21**:104–16.
55. Yin X, Zhou M, Zhang L, Fu Y, Xu M, Wang X, et al. Histone chaperone ASF1A accelerates chronic myeloid leukemia blast crisis by activating Notch signaling. *Cell Death Dis* 2022;**13**:842.
56. Wijayasinghe YS, Bhansali MP, Borkar MR, Chaturbhuj GU, Muntean BS, Viola RE, et al. A Comprehensive biological and synthetic perspective on 2-deoxy-d-glucose (2-DG), a sweet molecule with therapeutic and diagnostic potentials. *J Med Chem* 2022;**65**:3706–28.
57. Zahoor I, Suhail H, Datta I, Ahmed ME, Poisson LM, Waters J, et al. Blood-based untargeted metabolomics in relapsing-remitting multiple sclerosis revealed the testable therapeutic target. *Proc Natl Acad Sci U S A* 2022;**119**:e2123265119.